Non-recurrent Wideband Continuous Active Sonar

by

Jonathan B. Soli

Department of Electrical and Computer Engineering
Duke University

Date: _____

Approved:

_____
Jeffrey L. Krolik, Supervisor

_____
Loren W. Nolte

_____
Leslie M. Collins

_____
Donald B. Bliss

Thesis submitted in partial fulfillment of
the requirements for the degree of Master of Science in the Department of
Electrical and Computer Engineering in the Graduate School
of Duke University

2014

ABSTRACT

Non-recurrent Wideband Continuous Active Sonar

by

Jonathan B. Soli

Department of Electrical and Computer Engineering
Duke University

Date: _____

Approved:

_____
Jeffrey L. Krolik, Supervisor

_____
Loren W. Nolte

_____
Leslie M. Collins

_____
Donald B. Bliss

An abstract of a thesis submitted in partial
fulfillment of the requirements for the degree
of Master of Science in the Department of
Electrical and Computer Engineering in the Graduate School
of Duke University

2014

Abstract

The Slow-time Costas or "SLO-CO" Continuous Active Sonar (CAS) waveform shows promise for enabling high range and velocity revisit rates and wideband processing gains while suppressing range ambiguities. SLO-CO is made up of non-recurrent wideband linear FM chirps that are frequency staggered according to a Costas code across the pulse repetition interval. SLO-CO is shown to provide a near-thumbtack ambiguity functions with controllable sidelobes, good Doppler and range resolution at high revisit rates. The performance of the SLO-CO waveform was tested using the Sonar Simulation Toolset (SST) as well as in the shallow water Target and Reverberation Experiment 2013 (TREX13). For both the real and simulated results, the performance of the SLO-CO is compared to the conventional CAS waveform. Amplitude-Range-Velocity (ARV) processing of SLO-CO experimental trials reveal that relatively high direct blast sidelobes mask the target peak. Methods of suppressing the direct blast are discussed including adaptive filtering and re-designing the waveform.

Contents

List of Figures

Acknowledgements

I would like to thank Dr. Jeffrey Krolik for his support and direction over the last two and a half years. Also I would like to thank Dr. Loren Nolte, Dr. Leslie Collins, and Dr. Donald Bliss for serving on my master's committee. Special thanks to Dr. Granger Hickman and Itay Cnnan-on who laid the foundation for the work in this thesis and with whom I continue to actively collaborate.

Special thanks to Juan Ramirez Jr., my other fellow lab mates, and others who have offered me help during my time at Duke.

This work was supported by the Office of Naval Researche (ONR).

1

Introduction

Conventional active sonars use short, high-energy pulses or chirps to highlight targets with long delays between consecutive pulses or chirps to avoid range ambiguities. In this thesis, we present the Slow-time Costas Costas Coded (SLO-CO) waveform, a Continuous Active Sonar (CAS) waveform that is meant to be transmitted at 100% duty cycle with no delays between transmissions. The benefit of transmitting continuously is that it enables the potential for higher range and velocity revisit rates. The SLO-CO waveform was first introduced at the Oceans IEEE conference in 2012 by Hickman and Krolik [1].

The conventional CAS waveform consists of a long (e.g. 20 sec) Linear Frequency Modulated (LFM) chirp that is processed in narrowband segments via a Short Time Fourier Transform (STFT). The conventional CAS waveform and processing enable frequent range updates, but poor instantaneous velocity resolution. Because conventional CAS processing is narrowband, it has the undesirable effect of limiting gains due to pulse compression.

The SLO-CO waveform is made up of short LFM chirps that are frequency-staggered based on a circular Costas code. Frequency-staggered chirps are what

causes SLO-CO to be a Non-Recurrent Waveform (NRWF). Successful implementation of the SLO-CO waveform promises high range and velocity revisit rates as well as wideband processing gains. Costas frequency staggering mitigates range ambiguities that are commonly associated with other pulse-burst waveforms [2]. The Ambiguity Function (AF) of the SLO-CO waveform resembles the desirable thumbtack-like shape with a tall, narrow mainlobe with uniform delay and Doppler sidelobes.

The first reference in which the term NRWF was coined was written by Clancy et. al. in 1999 [3]. In this paper a Quadratic Phase Coding (QPC) was applied to a conventional LFM chirp train. It was shown that applying QPC reduced range ambiguities in the Over The Horizon (OTH) radar application. It was found that direct implementation of the QPC method to the CAS problem was not feasible. After some research, it was found that Costas codes could be used to achieve a non-recurrent waveform with good range and Doppler characteristics [4]. Costas frequency-staggered LFM chirps were first researched for radar by Levanon and Mozeson who coined the name "Modified Costas Signal" [5]. The use of circular Costas codes as well as the application to the continuous active sonar problem is what makes SLO-CO unique.

The performance of the SLO-CO waveform was tested in both computer simulations using the Sonar Simulation Toolset (SST) as well as in the Target and Reverberation Experiment 2013 (TREX13) sea trial. In simulation, SLO-CO performed as expected. However processing the TREX13 data was not as successful as anticipated. Recovery of the target in the experimental data was unsuccessful due to high sidelobes of the direct blast return. The direct blast is the direct path from the continually transmitting source to the array. The severity of this issue was not apparent in our simulations preceding the experiment.

Despite the setback, methods were investigated to recover the SLO-CO TREX13 results including applying an adaptive filter to mitigate the direct blast as well as

redesigning the waveform to reduce the overall sidelobe level. This thesis highlights each of these topics in Chapter 6.

Chapters 2 and 3 present a brief review of active sonar fundamentals and sonar waveform design. This motivates and lays the groundwork for discussing CAS and the concept of non-recurrent waveforms in Chapter 4. In Chapter 5 SST-simulated results of the SLO-CO waveform are presented. Chapter 6 presents the conventional CAS experimental results as well as highlighting the attempts made at recovering the TREX13 SLO-CO target. Chapter 7 presents ideas for future work and concludes this thesis.

2

Active Sonar for Target Detection

2.1 Target range and Doppler

Target range

The primary function of most sonars is to localize targets using acoustic data. In the active case, a waveform is transmitted using an underwater source. The acoustic waves propagate through the ocean until they reach an target that reflects the waves back towards the sonar where it is received by a single hydrophone or an array of hydrophones [6]. The time required for a pulse to propagate a distance r_0 and return off a reflective target (the 2-way propagation (echo) delay) is $t_0 = 2r_0/c$, where c is the propagation velocity in the medium. Therefore the target range is a function of t_0

$$r_0 = \frac{ct_0}{2} \tag{2.1}$$

The single hydrophone or multi-hydrophone array output is then processed to estimate the time delay t_0 and therefore the range of the specific target. This equation assumes that the medium is non-dispersive (constant c) and that the receiver and transmitting source are co-located which means the sonar is mono-static.

Target Doppler

Sonars can also used to measure a target's velocity. This can be especially useful when the goal is to track the target, or distinguish between moving and non-moving targets.

Assume that a target is in motion relative to the sonar. The relative motion will cause the echo return of the waveform to be Doppler shifted. For a target moving away from a Continuous Wave (CW) source with radial velocity v_0, the signal arriving at the target will observe the frequency

$$f_1 = f_0(1 - \frac{v_0}{c}) \tag{2.2}$$

where f_0 is the transmitted frequency, v_0 is the radial speed away from the source and c is the speed of sound. The reflected signal then undergoes an additional Doppler shift on the trip back to the sonar. The resulting received frequency in this 2-way case is

$$f_2 = f_0(\frac{1 - v_0/c}{1 + v_0/c}) \tag{2.3}$$

The Doppler shift is the difference between the received and transmitted frequencies:

$$\begin{aligned} f_d = f_2 - f_0 &= f_0(\frac{1 - v_0/c}{1 + v_0/c}) - f_0 \\ &= 2v_0\frac{f_0}{c + v_0} \end{aligned} \tag{2.4}$$

Because the speed of c underwater is likely much faster than the target speed, it is often assumed that $v_0 << c$, $(c + v_0) \rightarrow c$ allowing the approximation

$$f_d \approx 2v_0\frac{f_0}{c}. \tag{2.5}$$

From here, this model is utilized in the sonar's receive processing to estimate the target's radial velocity [6].

2.2 The simple pulse and Linear FM (LFM) chirp

The resolution of a sonar's range and velocity estimates are highly dependent on the transmitted waveform. Conventional Pulsed Active Sonars (PASs) use short (usually a second or less), high energy pulses or Linear Frequency Modulated (LFM) chirps to highlight targets. For now we will define the expressions for the simple pulse and LFM chirp and in Chapter 3 we will compare their performance.

The simple pulse

The expression for a simple narrowband pulse waveform of duration T and unity amplitude is:

$$s_p(t) = \text{rect}(\frac{t - T/2}{T})e^{j2\pi f_c t} \tag{2.6}$$

where f_c is the carrier frequency of the pulse. In this case, the rectangular function is defined by

$$\text{rect}(t) = \begin{cases} 1, & |t|<1/2 \\ 0, & \text{otherwise} \end{cases} \tag{2.7}$$

The resulting waveform is a finite duration sinusoid. In analysis, the simple pulse is often approximated by its rectangular envelope to simplify the mathematics. A cartoon example of this simple pulse in the time and frequency domain is shown in Fig. 2.1.

The LFM Chirp

The expression for an LFM chirp of duration T and unity amplitude is:

$$s_{LFM}(t) = \text{rect}(\frac{t - T/2}{T})e^{j2\pi f_0 t}e^{j\pi\mu t^2} \tag{2.8}$$

where f_0 is the nominal frequency and $B = \mu T$ is the swept bandwidth and μ is the LFM sweep rate in Hz/sec. The instantaneous frequency can be determined by

taking the derivative of the phase function, $\phi(t) = 2\pi f_0 t + \pi \mu t^2$:

$$f_i = \frac{1}{2\pi}\frac{d\phi(t)}{dt} = \mu t + f_0 \tag{2.9}$$

When μ is positive, instantaneous frequency increases with time and the pulse considered to be an *upchirp*. When μ is negative, instantaneous frequency decreases with time and the pulse is considered to be a *downchirp*. An example of the LFM upchirp in the time and frequency domain is also shown in Fig. 2.1.

2.3 Matched Filtering

Conventional processing of the received echo return involves the use of one or more matched filters to determine estimates of range and/or velocity. There are a number of components included in this received signal including but not limited to:

1. Direct path target echo return
2. Multi-path target echo returns
3. Ocean surface, bottom, and volume reverberations
4. Ocean noise
5. Electronic noise

Matched filters often are used to process received sonar signals because they maximize the output Signal-to-Noise Ratio (SNR), assuming that the non-signal components are simple Additive White Gaussian Noise (AWGN). The sum of the non-signal components in a real ocean environment will likely never be AWGN. However matched filters are still widely used due to their simplicity and robust performance without requiring a-priori information about the non-signal components. If prior information is available about the non-signal components, a whitening filter can be applied to

flatten the interference or noise spectra to make them look more like AWGN. However the whitening operation also modifies the signal spectrum in the process. Changes to the signal can be accounted for adjusting the matched filter appropriately. Whitening is addressed thoroughly in this document, but an example of whitening using vector notation can be found in Kay's first volume [7].

A derivation of the matched filter is shown below. This particular derivation follows a lecture from Dr. Nolte's Signal Detection and Estimation Theory course at Duke [8].

Goal Criterion: Maximize Output $SNR = R_0$ at $t = t_1$

Define:

$X(j\omega) = \int_{-\infty}^{\infty} x(t)e^{-j\omega t}\,dt$: Fourier Transform (FT)

$x(t) = \int_{-\infty}^{\infty} X(j\omega)e^{j\omega t}\,d\omega$: Inverse Fourier Transform (IFT)

$s(t) \xrightarrow{F.T.} S(j\omega)$: Frequency spectrum of input signal (Echo return)

$h(t) \xrightarrow{F.T.} H(j\omega)$: Frequency spectrum of unknown linear system

$s_o(t) \xrightarrow{F.T.} S_o(j\omega)$: Frequency spectrum of output signal

$R_o = |S_o(t_1)|^2/\mathbb{E}[N_o^2(t)]$: Output SNR

Assuming a Linear Time Invariant (LTI) system,

$S_o(j\omega) = H(j\omega)S(j\omega)$ and also $s_o(t_1) = \frac{1}{2\pi}\int_{-\infty}^{\infty} H(j\omega)S(j\omega)e^{j\omega t_1}\,d\omega$

Now assuming that the noise is Wide Sense Stationary (WSS) at the input, so the output is also WSS:

$$\frac{1}{2\pi}\int_{-\infty}^{\infty} S(j\omega)|H(j\omega)|^2 e^{j\omega t}\,d\omega\bigg|_{t=0} = \mathbb{E}[N_o^2(0)] = R_{N_o}(0) \tag{2.10}$$

Now assuming that the noise is white, mean $\mu = 0$ and constant spectral density $N_0/2$, we have that the output SNR is:

$$R_o = \frac{|S_o(t_1)|^2}{\mathbb{E}[N_o^2(t)]} = \frac{|\frac{1}{2\pi}\int_{-\infty}^{\infty} S(j\omega)H(j\omega)e^{j\omega t_1}\,d\omega|^2}{\frac{N_0}{2}\int_{-\infty}^{\infty}|H(j\omega)|^2\,d\omega} = \frac{|\int_{-\infty}^{\infty} S(j\omega)H(j\omega)e^{j\omega t_1}\,d\omega|^2}{\pi N_0\int_{-\infty}^{\infty}|H(j\omega)|^2\,d\omega} \tag{2.11}$$

Now we need to solve for $H(j\omega)$ that maximizes R_0. Recall a form of the Cauchy-Schwarz Inequality:

$$\left|\int_{-\infty}^{\infty} Q_1(j\omega)Q_2(j\omega)\,d\omega\right|^2 \leqslant \int_{-\infty}^{\infty}|Q_1(j\omega)|^2\,d\omega\int_{-\infty}^{\infty}|Q_2(j\omega)|^2\,d\omega \tag{2.12}$$

with equality if $Q_1(j\omega) = kQ_2(j\omega)$, where k is an arbitrary factor. From here we examine the numerator of R_0 and substitute $Q_1(j\omega) = H(j\omega)$ and $Q_2(j\omega) = S(j\omega)e^{j\omega t_1}$ into the Schwarz Inequality to get:

$$R_0 \leqslant \frac{\int_{-\infty}^{\infty}|H(j\omega)|^2\,d\omega\int_{-\infty}^{\infty}|S(j\omega)e^{j\omega t_1}|^2\,d\omega}{\pi N_0\int_{-\infty}^{\infty}|H(j\omega)|^2\,d\omega} = \frac{1}{\pi N_0}\int_{-\infty}^{\infty}|S(j\omega)e^{j\omega t_1}|^2\,d\omega \tag{2.13}$$

Using the equality condition from the Schwarz inequality, we find the optimal filter that maximizes output SNR at $t = t_1$ in AWGN to be:

$$H_{opt}(j\omega) = k'S^*(-j\omega)e^{-j\omega t_1} \xrightarrow{I.F.T.} h_{opt}(t) = k's^*(t_1 - t) \tag{2.14}$$

The impulse response of this filter is a "flipped in place" version of the original transmitted waveform. Note that the matched filtering operation is the optimal solution in the case of AWGN, regardless of the transmitted waveform. Fig. 2.1 shows a cartoon version of the matched filtering process for the simple pulse and LFM chirp waveforms.

Notice how the output of the matched filter of the simple pulse is a triangle. The triangle response for the pulse is intuitive, because it is the convolution of two

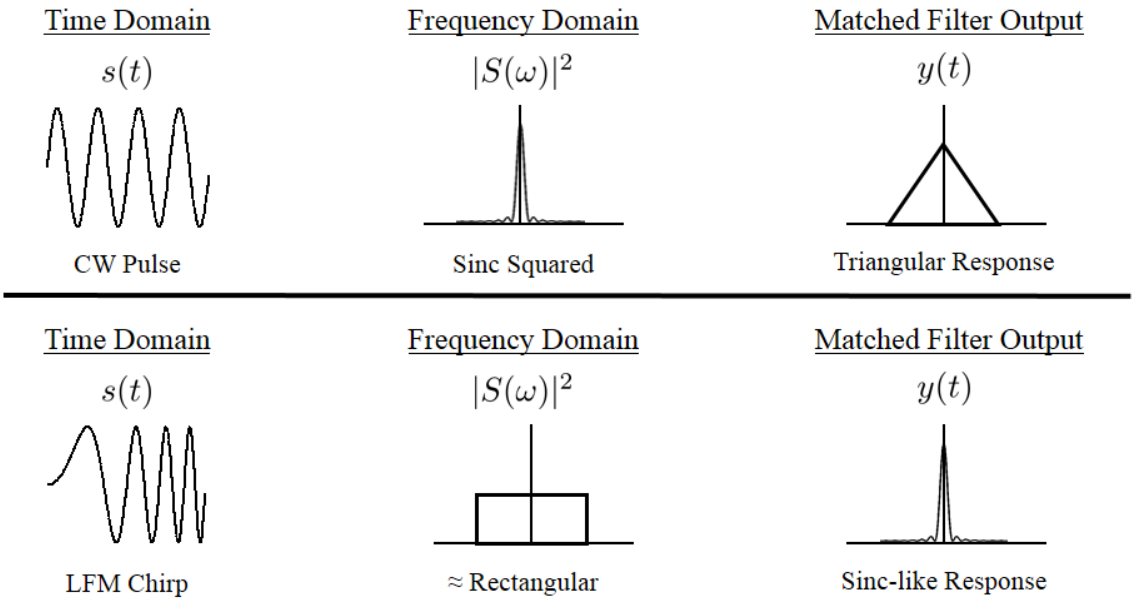

FIGURE 2.1: (Top) A simple pulse in time and frequency domain as well as its corresponding matched filter response. (Bottom) An LFM up-chirp in time and frequency domain as well as its sinc-like matched filter response.

rectangular pulses. It is also intuitive that width of the base of this triangle is $2T$. The sinc-like response of the LFM chirp is due to pulse compression. More information on this topic can be found in Chapter 3.

Estimating target range from the matched filter output

The matched filter was designed to maximize the output SNR at a particular time instant t_1. Natural questions may be: How should t_1 be chosen? How is the target range related to the matched filter output?

We start by choosing $t_1 = T$, where T is length of the pulse/chirp. Now suppose that $s(t)$, the input to the matched filter, is an echo return from a target at an unknown range r_0, corresponding to the time delay $t_0 = 2r_0/c$ as described in the Section 2.1; the output of the matched filter will be the convolution integral:

$$y(t) = \int_{-\infty}^{\infty} s(t - t_0)k's^*(\xi + T - t)\, d\xi \tag{2.15}$$

This is the correlation of the received, delayed echo and the matched filter impulse response. $y(t)$ will have the same shape as before (a triangle in the pulse case or a sinc in the chirp case), but its peak will be located at $t_{peak} = t_1 + T$. From here the target range can be easily calculated using Eq. 2.1.

Estimating target velocity from the matched filter output

Now suppose that the target is moving and we are using the simple pulse as our waveform. In Section 2.1 it was shown that if a target has a radial velocity v_0 relative to the sonar, the resulting Doppler shift will be $f_d \approx 2v_0\frac{f_c}{c}$, where f_c is the carrier frequency of the pulse. To match filter an echo return with an imposed Doppler shift, we must also impose a Doppler shift on the matched-filter replica resulting in

$$h_d(t) = k's^*(-t)e^{j2\pi f_d t} \xrightarrow{F.T.} H_d(j\omega) = k'S^*(\omega - 2\pi f_d) \tag{2.16}$$

A more interesting and practical scenario is when v_0 is unknown. Here a bank filters, each adjusted for a different Doppler shift hypothesis are applied in parallel to the same received signal. Then the filter with the closest match to the actual Doppler shift of the target should achieve the highest peak in its output. Because each Doppler shift can be mapped to a corresponding target velocity, the highest peak will correspond to the filter with the closest f_d and therefore hypothesized velocity estimate.This leads to the topic of Doppler sensitivity of a given waveform. Doppler sensitivity is characterized by how sensitive a particular waveform is to Doppler mismatch of its (mis)matched filter. This concept is explained in more detail in Chapter 3.

2.4 Binary hypothesis testing

In conventional sonars, the matched filter output is often passed into a binary hypothesis detector. To limit the scope of this paper, we only briefly highlight the

concepts behind binary hypothesis testing. More detailed information can be found in Kay's second volume [9]. A schematic diagram of such a detector is shown in the Fig. 2.2 below. Note that these steps can be performed in either the time or frequency domain.

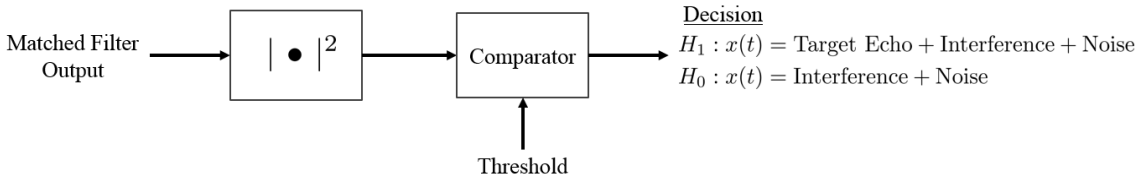

FIGURE 2.2: Processing chain for a binary hypothesis detector for a conventional sonar starting at its matched filter output.

The purpose of the binary hypothesis detector in to make a binary decision as to whether or not a target echo is present in the data. As mentioned in the beginning of this section, the received signal will be the sum of multiple components including the signal, interference, and noise. These components will also be included in the matched filter output. The component of the matched filter output corresponding to these components is often called the background level. The matched filter response of the target echo component should result in a peak, that if strong enough, rises above the background. Because there is often uncertainty associated with the interference and noise model, statistical techniques are utilized.

Now we examine Fig. 2.2 above. In our case, H_1 denotes the hypothesis that the target echo is present in the data and H_0 denotes the hypothesis that a target echo is not present in the data. Probability distributions for $P(x(t)|H_0)$ and $P(x(t)|H_1)$ can be developed by modeling the problem or by gathering experimental data. Once $P(x(t)|H_0)$ and $P(x(t)|H_1)$ are available, Receiver Operating Characteristic (ROC) plots of Probability of Detection (P_d) vs Probability of False alarm (P_F) can be made. ROC curves characterize the performance of the detector given all different

threshold levels. Once the ROC is obtained, a reasonable operating point (P_d', P_f') can be chosen and its associated threshold is determined. Once an appropriate threshold is determined, the detector can be implemented.

Often the output of the binary hypothesis detector is then linked to some sort of user interface (e.g. detected target range vs. time image, etc) that is interpreted by the sonar operator. Given the threshold is set correctly and $P(x(t)|H_0)$ and $P(x(t)|H_1)$ accurately model the true scenario, the detector should perform within the specifications defined by the operating point.

3

Ambiguity Functions and Waveform Design

3.1 The Ambiguity Function (AF)

The Ambiguity Function (AF) is a tool for waveform design that characterizes the behavior of a waveform paired with its matched filter. AFs are useful when trying to examine delay and Doppler resolution, sensitivity, sidelobe levels, and range-Doppler coupling [2]. There are both wideband and narrowband versions of the ambiguity function. The narrowband version often leads to simpler closed-form AFs, however the narrowband assumption is invalid if the bandwidth of the transmitted signal is a considerable fraction of the mean signal frequency [10].

Here we define the wideband Kelly-Wishner version of the complex ambiguity function

The wideband complex AF

$$\overline{AF}_{WB}(t,\beta) \equiv \int_{-\infty}^{\infty} s(t)s^*(\beta(\xi - t))d\xi \tag{3.1}$$

where $s(t)$ is the waveform of interest, t is the time delay relative to the expected matched filter peak location and $\beta = \frac{1+v_0/c}{1-v_0/c}$ and in most cases, $c >> v_0$ makes

$\beta \approx 1 - 2v_0/c$ where v_0 is velocity mismatch between the replica and received versions of the signal [11]. β is a time scaling (expansion or compression) factor that accounts for the velocity of the target. The derivation of β is immediately apparent after inspecting Eq. 2.2.

In the narrowband case, β is replaced with a simple Doppler shift term. The narrowband Woodward version of the complex ambiguity function in both time and frequency domain is defined below [12].

The narrowband complex AF

$$\overline{AF}(t, f_d) = \int_{-\infty}^{\infty} s(t)s^*(\xi - t)e^{j2\pi f_d \xi}\, d\xi = \int_{-\infty}^{\infty} S^*(\omega)S(\omega - 2\pi f_d)e^{j\omega t}\, d\omega \tag{3.2}$$

Here f_d is the mismatch between the design Doppler shift and the one actually received which is analogous to β in the wideband case. Also note that $S(\omega)$ denotes the Fourier Transform of $s(t)$.

The *true* ambiguity function is the magnitude of the complex ambiguity function or

$$AF(t, f_d) = |\overline{AF}(t, f_d)| \tag{3.3}$$

The AF surface is often displayed as a 3-dimensional plot. It can also be informative to visualize cuts across the surface holding either t or f_d constant. $AF(t, 0)$ is the zero-Doppler "cut" and is intuitively just the matched filter output of the waveform. The zero-Doppler cut is useful when investigating delay-related properties such as delay resolution, range sidelobe, and ambiguity levels. $AF(0, f_d)$ is the zero-delay cut shows the waveform's sensitivity to Doppler mismatch. The zero-delay cut is useful when investigating Doppler/velocity-related properties such as Doppler resolution and Doppler ambiguity levels.

There many specific AF properties. A complete review along with proofs can be found in "Radar Signals" by Levanon [13]. The three most relevant to understanding

this thesis are defined below. The first property states that if the waveform has energy E, then

$$|AF(t, f_d)| \leqslant |A(0,0)| = E \tag{3.4}$$

This dictates that a peak equal to the waveform energy will occur at the origin. This peak corresponds to a filter matched exactly in delay and Doppler.

The second property states that the total area under any ambiguity surface is constant and is given by

$$\int_{-\infty}^{\infty} \int_{-\infty}^{\infty} |AF(t, f_d)|^2 \, dt \, df_d = E^2 \tag{3.5}$$

This implies that it is impossible to eliminate ambiguity, but it is possible re-organize the ambiguity surface. Ambiguity is moved around the surface by varying the waveform. This will become more evident once we examine the SLO-CO waveform and how it results in distributing the ambiguity in a particularly desirable manner.

The third property is that all AFs are symmetric or

$$AF(t, f_d) = AF(-t, -f_d) \tag{3.6}$$

Intuitively, the ideal shape of the AF is usually considered to be a "thumbtack" with a single peak centered at $AF(0,0)$ and the rest of the energy distributed evenly across range and Doppler [2]. A narrow central peak implies good resolution in both range and Doppler. The uniformity of the rest of the surface implies that there are no pronounced range or Doppler ambiguities.

3.2 The AF of the simple pulse

Consider a simple pulse centered on the origin with unit energy, $E = 1$

$$s_p(t) = \frac{1}{\sqrt{T}} \qquad -T/2 \leqslant t \leqslant T/2 \tag{3.7}$$

Applying Eq. 3.2 with and changing the limits of integration so that $T > 0$ we have the narrowband complex AF

$$\begin{aligned}
\overline{AF}(t, f_d) &= \int_{-T/2+t}^{T/2} \frac{1}{T} e^{j2\pi f_d \xi}\, d\xi \qquad \text{let } u = j2\pi f_d \\
&= \frac{1}{T} \int_{-T/2+t}^{T/2} e^{u\xi}\, d\xi \\
&= \frac{e^{uT/2} - e^{u(t-T/2)}}{uT} \qquad \text{manipulate and plug back in } u \\
&= \frac{sin(\pi f_d (T - t))}{\pi f_d T} e^{j f_d t}
\end{aligned} \tag{3.8}$$

Resulting in the true AF

$$AF(t, f_d) = |\overline{AF}(t, f_d)| = \left| \frac{sin(\pi f_d (T - |t|))}{\pi f_d T} \right| \qquad -T \leqslant t \leqslant T \tag{3.9}$$

The zero Doppler cut after applying L'Hospital's rule becomes:

$$AF(t, 0) = \frac{T - |t|}{T} \qquad -T \leqslant t \leqslant T \tag{3.10}$$

and the zero-delay cut gives the matched filter output with the expected peak at $t = 0$

$$AF(0, f_d) = \left| \frac{sin(\pi f_d T)}{T \pi f_d} \right| \tag{3.11}$$

Fig. 3.1 below shows plots of the AF of the simple pulse, as well as the zero Doppler and zero delay cuts in both linear and dB scales.

Range resolution of the simple pulse

Notice how in the zero-Doppler cut, the output is a triangular function of width $2T$. This corresponds to the Raleigh (null-to-null) time delay resolution of simple pulse

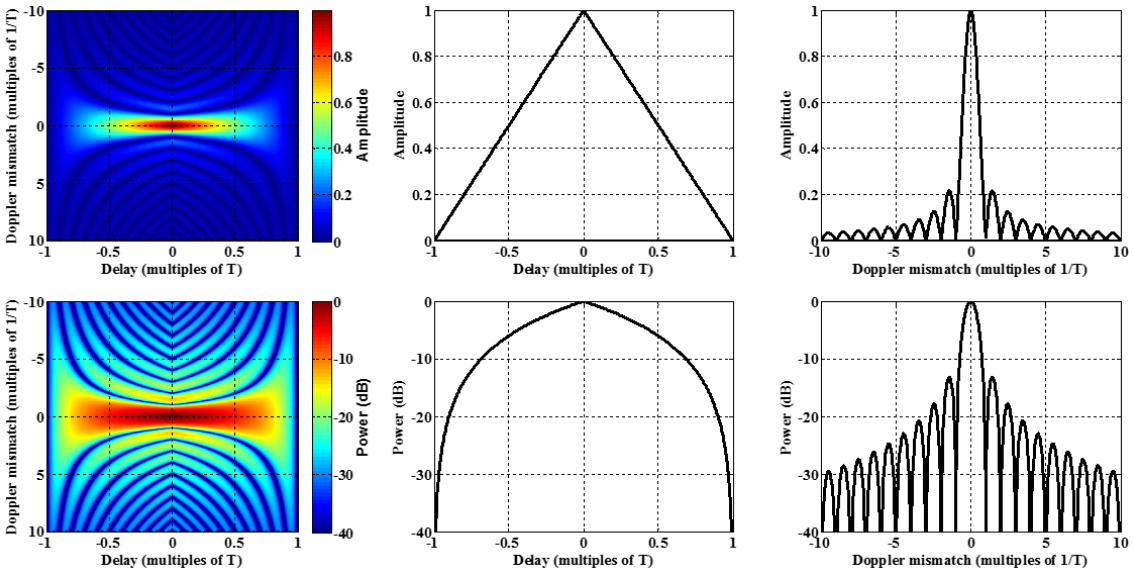

FIGURE 3.1: (Top 3) From left to right, the AF, the zero Doppler cut, and the zero delay cut (matched filter output) of the simple pulse waveform. (Bottom 3) The same plots as the top 3, but in units of Decibels.

waveform. This time delay resolution relates directly to the 2-way range Raleigh resolution of the simple pulse

$$\Delta R = \frac{cT}{2} \qquad m \tag{3.12}$$

The range resolution is the minimum distance between two targets that still allows to distinguish between them. The range resolution of the simple pulse is relatively poor in comparison to pulse compression waveforms like the LFM chirp. For a simple pulse of duration 0.5 seconds emitted underwater ($c = 1500$ m/s) the Raleigh resolution is found to be

$$\begin{aligned} \Delta R_0 &= \frac{(1500 \text{ m/s})(0.5 \text{ sec})}{2} \\ &= 375 \qquad m \end{aligned} \tag{3.13}$$

This means that if two targets are spaced less than 375 m apart, it may be impossible to distinguish between them using a 0.5 sec simple pulse as our waveform. It is also

important to keep in mind that the energy of a pulse is also proportional to its duration. Therefore the only way to increase the transmitted energy is by elongating the pulse simultaneously destroys the range resolution. We see that the LFM chirp waveform overcomes this issue because it is a pulse compression waveform.

Velocity resolution of the simple pulse

Notice that the Doppler mismatch plot forms a sinc function with the first null at $1/T$. This is considered to be the Raleigh Doppler resolution of the simple pulse.

$$\Delta f_d = \frac{1}{T} \qquad Hz \tag{3.14}$$

Plugging this into the equation in Section 2.1 which related the targets velocity to the Doppler shift gives us that the velocity resolution (with $v_0 << c$) is

$$\begin{aligned} \Delta f_d = \frac{1}{T} = 2\Delta v \frac{f_0}{c} \\ \\ \Rightarrow \Delta v = \left| \frac{1}{2T} \frac{c}{f} \right| \\ = \left| \frac{\lambda}{2T} \right| \end{aligned} \tag{3.15}$$

The velocity resolution is the minimum velocity difference between two targets that still allows to distinguish between them. In most cases, $1/T$ is considered to be a fairly large Doppler shift [2]. This means that the simple pulse is relatively tolerant to Doppler/velocity mismatch. This essentially means that the main lobe width in the Doppler spectrum is wide. This comes at the cost of the Doppler resolution being poor. This is similar to the trade-off between main lobe width and Side Lobe Level (SLL) in filter design. This can also be related back to the energy conservation property of AFs.

3.3 The AF of the LFM chirp

In this section, we derive the narrowband AF of the LFM chirp and discuss the resulting range resolution and velocity resolution. It will be shown that by using LFM chirps, the range resolution is much better than the simple pulse while the velocity resolution stays the same.

The derivation for the AF for the LFM chirp by direct calculation is a bit more tedious than the simple pulse. Instead, we introduce another AF property called the shearing property which effectively adds the linear frequency modulation to the result derived for the simple pulse. The derivation for the shearing property can be found in Levanon's Radar Signals [13].

We start by defining a modified waveform $s'(t)$ by adding LFM to $s(t)$:

$$s'(t) \equiv s(t)e^{j\pi\mu t^2} \tag{3.16}$$

The shearing property is

$$AF'(t, f_d) = AF(t, f_d + \mu t) \tag{3.17}$$

where $AF(t, f_d)$ is the ambiguity function of the unmodulated $s(t)$. The reason this is called the shearing property is because adding LFM causes the triangular shape of the simple pulse to be sheared in the delay-Doppler plane of the AF. This is evident in the AF plots of the LFM signal.

Applying the shearing function to the simple pulse returns the ambiguity function of the LFM chirp:

$$AF(t, f_d) = \left| \frac{sin(\pi(f_d + \mu t)(T - |t|))}{T\pi(f_d + \mu t)} \right| \qquad -T \leqslant t \leqslant T \tag{3.18}$$

The zero Doppler response is

$$AF(t, 0) = \left| \frac{sin(\pi\mu t(T - |t|)}{T\pi\mu t} \right| \qquad -T \leqslant t \leqslant T \tag{3.19}$$

and the zero delay response is

$$AF(0, f_d) = \left| \frac{sin(T\pi f_d)}{T\pi f_d} \right| \tag{3.20}$$

The ambiguity function, the zero Doppler cut, and the zero delay cut with $BT = 10$ plotted in dB are shown in Fig 3.2.

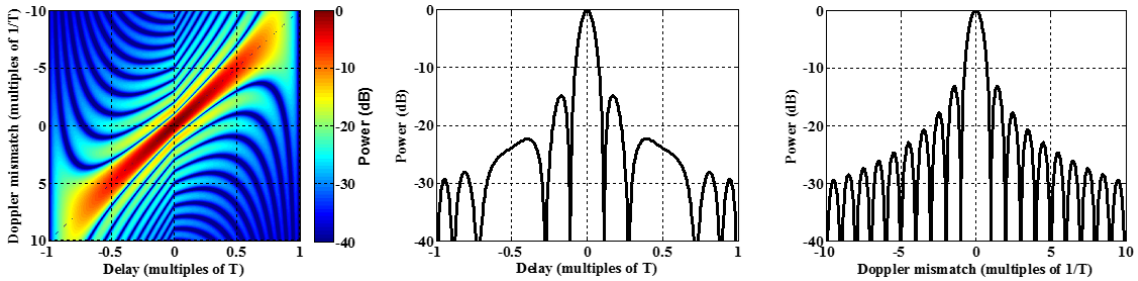

FIGURE 3.2: From left to right, the AF, the zero Doppler cut, and the zero delay cut (matched filter output) of the LFM chirp waveform with $BT = 10$.

This is the simpler narrowband version of the LFM chirp. A detailed version of the wideband version can be found in Zhen-biao's "Wideband ambiguity function of broadband signals" [10].

Range resolution of the LFM chirp

Notice that in the LFM case, the zero-Doppler cut looks roughly sinc-like as opposed to the triangle shape for the simple pulse. By inspecting Eq. 3.19, we notice that the first null should occur where the argument of sine in the numerator is equal to π.

$$AF(t, 0) = \left| \frac{sin(\pi\mu t(T - |t|)}{T\pi\mu t} \right| \qquad -T \leqslant t \leqslant T \tag{3.21}$$

which occurs when $\mu T(T - |t|) = 1$. If we define $B = \mu T$ to be the swept bandwidth of the LFM, we get $B(T - |t|) = 1$ which for positive t this becomes

$$Bt - \frac{Bt^2}{T} = 1 \Rightarrow t^2 - Tt + T/B = 0 \tag{3.22}$$

The positive root of this equation occur at $t = (T - \sqrt[2]{T^2 - 4T/B})/2 = T(1 - \sqrt[2]{1 - 4/BT})/2$. We can simplify this result by using the series expansion of the square root

$$\sqrt[2]{1-x} = 1 - \frac{x}{2} - \frac{x^2}{8} - \cdots \approx 1 - \frac{x}{2} \qquad x << 1 \tag{3.23}$$

plugging in our result returns

$$t \approx \frac{T}{2}[1 - (1 - \frac{2}{BT})] \approx \frac{1}{B} \qquad BT >> 1 \tag{3.24}$$

Thus the Raleigh resolution in time is approximately $1/B$ seconds. This makes the Raleigh range resolution for the LFM chirp [2]

$$\Delta R = \frac{c}{2B} \qquad m. \tag{3.25}$$

Here we note that the range resolution of the LFM chirp is now only dependent on the swept bandwidth and the constant c, instead of T. This effect is due to pulse compression that is explained in Section 3.4.

Velocity resolution of the LFM chirp

If we compare Eq. 3.11 and 3.20, we see that the zero-delay cut of the ambiguity function is the same for both the simple pulse and the LFM chirp. Therefore the Raleigh velocity resolution of the LFM chirp is also

$$\Delta v = \left| \frac{\lambda}{2T} \right| \tag{3.26}$$

3.4 Pulse compression

The basic concept behind pulse compression is illustrated by the Fig. 3.3. The notion behind pulse compression is that the transmitted energy contained in a long duration low power pulse (gray) can be comparable to a short duration high power pulse

(red). Note that signal energy is preserved throughout pulse compression processing or $PT = P_{\text{comp}}T_{\text{comp}}$.

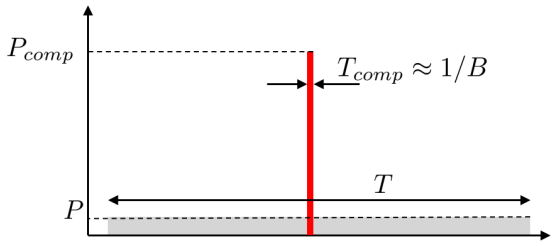

FIGURE 3.3: Comparison of the energy distribution of a waveform before and after pulse compression processing

In Fig. 3.3, the gray box indicates a relatively low-power, long duration received target signal of bandwidth B. This signal is then pulse-compressed in the receiver which effectively uses the bandwidth of the signal to compress the energy into a shorter duration, higher signal that is indicated in red. Some common examples of pulse-waveforms include LFM chirps, Hyperbolic Frequency Modulated (HFM) chirps, binary phase-coded, and multi-phase coded waveforms.

We use LFM chirp as an illustrative example. It was shown that the zero-Doppler cut of the AF of the LFM waveform is approximately a sinc function whose mainlobe width approximately $1/B$. This intuitively makes $T_{comp} \approx 1/B$. Because energy is conserved through pulse compression, this causes the level of the pulse-compressed peak to be approximately

$$\begin{aligned} P_{\text{comp}} &= \frac{T}{T_{\text{comp}}} P \\ &\approx (\frac{T}{1/B}) P \\ &= TBP \end{aligned} \tag{3.27}$$

Pulse compression is achieved by modulating the transmitted pulse (e.g. LFM) and then correlating (match filtering) the received signal with the transmitted pulse

[2]. Assuming AWGN, the post-processing level of the noise will not change because it is uncorrelated with the transmitted signal. So after pulse compression, the power of the received signal can be considered to be amplified by TB, the time-bandwidth product of the signal. Additionally, the range resolution of the system has also been drastically improved.

3.5 Pulse burst waveforms

Pulse burst waveforms involve sending multiple pulses or chirps in succession. They are often used to improve velocity resolution. They do so, because the frequency resolution of the measured f_d is proportional to the observation time of the sinusoid at that frequency. Assuming that there are only small changes in target velocity between successive pulses/chirps, it is intuitive that more observed pulses/chirps leads to longer observation time which leads to better Doppler resolution. The pulse burst waveform is defined as:

$$s_{pb}(t) = \sum_{m=0}^{M-1} s_{sp}(t - mT_{PRI}) \tag{3.28}$$

where $s_{sp}(t)$ is a single pulse of duration T, M is th number of pulses, and T_{PRI} is the Pulse Repetition Interval (PRI). Note that $s_{sp}(t)$ does not necessarily have to be a simpule pulse waveform and can be replaced by any other "kernel" waveform (e.g. an LFM chirp). Fig. **??**shows an examples of the simple pulse and LFM burst waveforms.

Processing pulse burst waveforms is often performed pulse-by-pulse which involves match filtering each individual received pulse, time aligning their responses, and then summing their responses coherently.

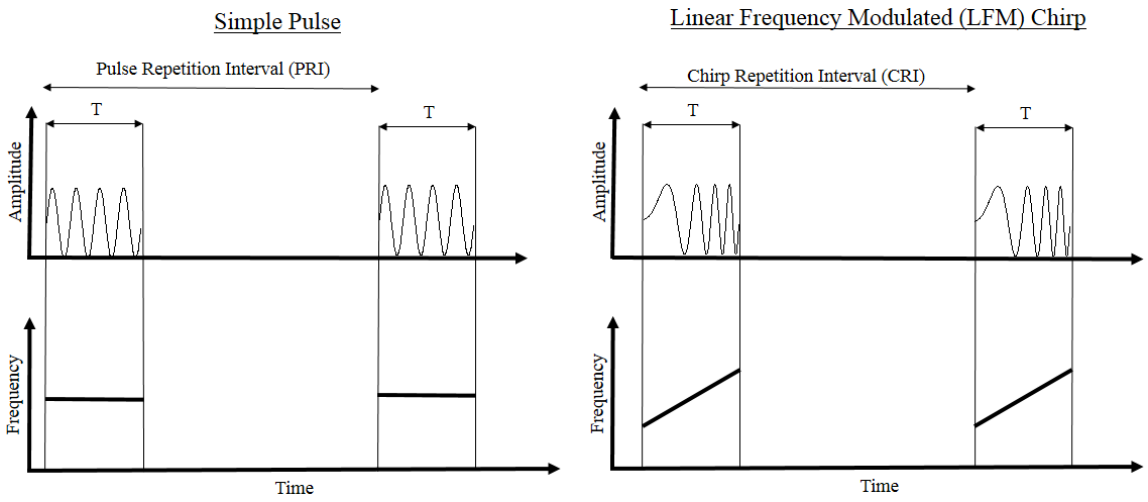

FIGURE 3.4: (Left) The simple pulse burst waveform in time and frequency domain. (Right) The LFM chirp burst waveform in time and frequency domain.

3.5.1 Range-folding of pulse burst waveforms

A cartoon example of the simple pulse burst waveform with $M = 3$ reflecting off a target at range $r_0 = \frac{cT_{PRI}}{2}$ and its corresponding matched filter output is shown in the Fig. 3.5.

As annotated in the image, the sub-peaks or "ghost targets" in the matched filter output known as range ambiguities occur at integer multiples of the Pulse Repetition Interval (PRI) [2]. They are the result of correlating $< M$ pulses of the waveform with the echo return whereas the main peak corresponds to the correlation of all M pulses. In the presence of interference and noise it is usually difficult to distinguish the true target peak from ambiguous returns. As one might expect, range ambiguities also appear in the ambiguity functions of pulsed waveforms. This leads to the well-known "bed of nails" AF structure of conventional pulsed radar systems.

In conventional Pulsed Active Sonar (PAS), the issue of range ambiguities is overcome by setting the delay between subsequent transmissions very long. Often underwater targets of interest may be many kilometers away. Assuming $c = 1.5$ km/s

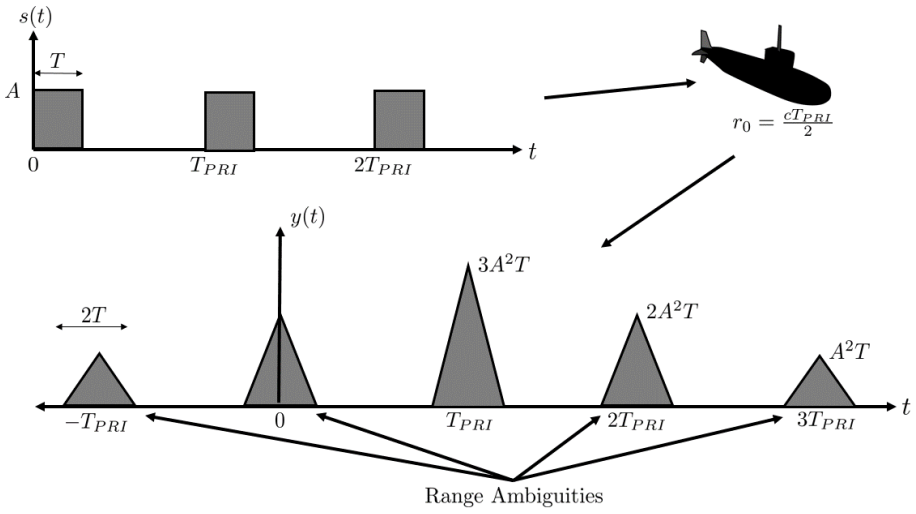

FIGURE 3.5: Cartoon of pulse-by-pulse processing of a simple pulse burst waveform. (Top) Pulse burst waveform, $M = 3$. (Bottom) Pulse burst matched filter output resulting from a target located at range $r_0 = \frac{cT_{PRI}}{2}$.

and $r_0 = 10$ km the resulting $t_0 = \frac{2(10 \text{ km})}{1.5 \text{ km/s}} \approx 13.3$ seconds. In this case, the PRI would have to be longer than 13.3 seconds. Thus the sonar operator would have to wait at least 13.3 seconds before receiving new range and/or velocity updates. The rest of this document will consider Continuous Active Sonar (CAS) waveforms that are designed to transmit continuously while simultaneously suppressing range ambiguities down to a reasonable level.

4

Continuous Active Sonar (CAS)

In all prior sections of this thesis, we have discussed Pulsed Active Sonars (PASs) that use short, high energy pulses or chirp waveforms. A major downside to this type of waveform is the issue of range ambiguities or "ghost" targets that can severely limit the unambiguous range of the sonar. Traditionally long PRIs with long delays between transmissions are used to mitigate this issue, however this comes at the cost of low revisit rates.

Continuous Active Sonar (CAS) waveforms were developed to increase revisit rates by transmitting at 100% duty cycle (with no delay between consecutive transmissions). Given this framework, CAS requires that range ambiguities must be suppressed in some way which can be achieved by using a Non-recurrent Waveform (NRWF).

Another major consideration that must be taken into account for CAS is the direct blast. The direct blast is the signal that travels directly from the source to the receiver. In PAS systems the direct blast is not an issue, because the receiver can easily be range gated to not include the direct blast. In the CAS scenario, the

transmitter is sounding continuously so target echoes and direct blast returns are both present at all times in the received signal. Also, assuming the source in close proximity to the receiver, the direct blast will undoubtedly be the loudest component of the received signal. Therefore the direct blast must somehow separated from from the target signal before detection of weak targets is remotely possible. This is often achieved by spatially filtering the signal using an array of receivers or by other methods. More details on the direct blast issue are explained in Chapter 6.

4.1 Non-Recurrent Waveforms (NRWFs)

A non-recurrent waveform is one that transmits, but does not repeat itself over some long time interval. The NRWF concept can be understood as a pulse-burst waveform, where each pulse or chirp is unique in some way. Non-recurrent waveforms offer show promise for mitigating range folding issues, because if each transmitted pulse is different in some way (e.g. frequency or phase diversity), the inter-pulse correlation that corresponds to each "ghost target" peak may be drastically be reduced, while maintaining a much higher update rate than PAS systems.

There are a number of different ways to achieve sub-pulses/chirps diversity. Some common methods discussed in the literature involve PRI-staggering, frequency-staggering, or phase-coding each sub-pulse. Most of the researched methods of achieving NRWFs involve adjusting the staggering or coding according to a specific code that results in manipulating the ambiguity surface in some desirable way. Many common methods of achieving pulse diversity were tested for their feasibility of use in the CAS application before SLO-CO was developed. Many of the listed references correspond to these methods, but will not be discussed in detail in this thesis. The remainder of this chapter focuses on the conventional CAS and SLO-CO waveforms.

4.2 The conventional CAS waveform and processing

The conventional CAS waveform utilizes long ($\approx$ 20 sec) LFM chirps transmitted at 100% duty cycle. An example spectrogram of a single realization of the CAS waveform is shown in Fig. 4.1

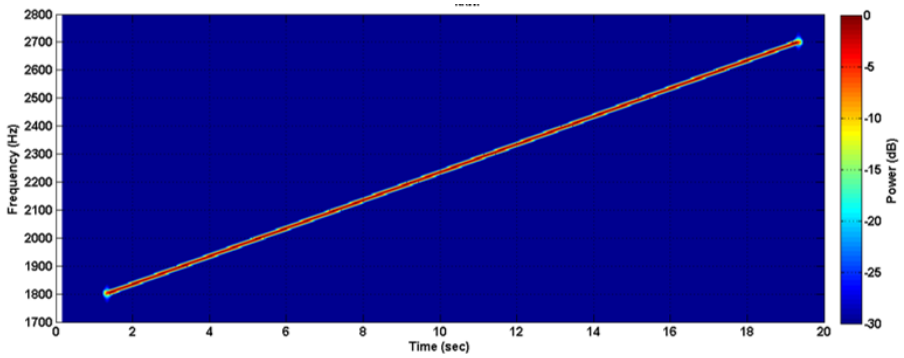

FIGURE 4.1: Example spectrogram of the conventional CAS waveform.

Conventional CAS processing is performed by de-chirping the received waveform and then taking the Short-Time Fourier Transform (STFT) of the de-chirped signal. De-chirping the received waveform is accomplished by multiplying the received waveform by a replica of the transmitted chirp. This causes delay difference between the received and replica signals to be converted into proportional frequency shifts. The left-most diagram in Fig. 4.2 helps illustrate the idea.

Next the STFT computed of a short interval of the de-chirped signal and its power is displayed. The result is a fast-update display of range vs. time. The range resolution is determined by the binwidth of the narrowband STFT. A diagram of the CAS processing chain is shown in Fig. 4.2.

4.2.1 Conventional CAS viewed as a NRWF

The CAS waveform can be viewed as a non-recurrent waveform by breaking it up into a number of unique narrowband chirps sub-chirps as shown in Fig. 4.3.

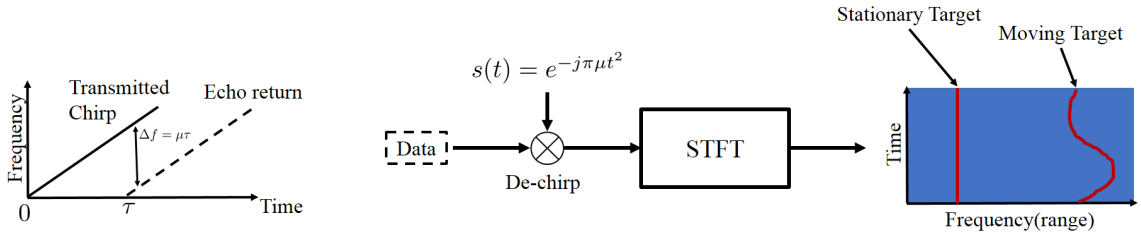

FIGURE 4.2: Conventional processing chain for the conventional CAS waveform.

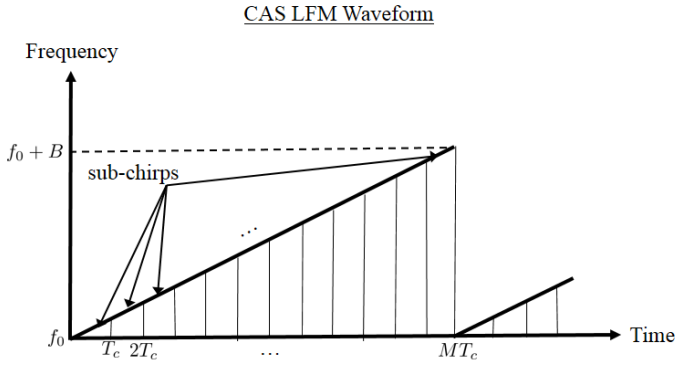

FIGURE 4.3: Time-frequency plot viewing the conventional CAS waveform as non-recurrent.

The expression for the CAS waveform with bandwidth B and duration T viewed in its non-recurrent form is

$$s_{CAS}(t) = \sum_{m=0}^{M-1} a_m(t) rect(\frac{t - mT_c}{T_c}) e^{j\pi k_c (t - mT_c)^2} \tag{4.1}$$

where M is the number of sub chirps $T_c = T/M$ is the duration of each sub-chirp, $k_c = \frac{B}{MT_c}$ is the sweep rate of each chirp and $a_m(t) = e^{j\pi k_c m T t}$. The $a_m(t)$ term adds the a frequency offset of $\pi k_c T_c$ to each sub-chirp which aligns them to be one long LFM chirp. The CAS waveform viewed in this way exposes how frequency diversity is used to make each sub-chirp unique and mitigate the issue of range folding in standard pulse-burst waveforms.

This CAS waveform and the processing method obtains frequent range estimates without the issue of range folding but has poor instantaneous velocity resolution.

Really the only way of achieving useful velocity estimates from CAS is by determining the rate of change of consecutive range estimates. Sacrificing instantaneous Doppler/velocity estimates can cause major issues when trying to discriminate a moving target from non-moving clutter/reverberation. In many environments, especially in shallow water, the clutter may be a very strong component of the received signal.

Another negative aspect of conventional CAS is that the processing is narrowband. As explained in Section 3.4, the gains obtained due pulse compression are proportional to the bandwidth of the signal. Therefore narrowband processing has the undesirable effect of limiting these gains. The SLO-CO waveform presented in the next section does not have this issue because its processing is wideband.

4.3 The Slow-time Costas-Coded (SLO-CO) NRWF

The SLO-CO waveform was developed to enable range *and* velocity estimates at high revisit rates while suppressing range ambiguities. SLO-CO also offers wideband processing gains that conventional CAS does not.

The design process of this of the SLO-CO waveform started with the investigation of using NRWF waveforms from Over-The-Horizon (OTH) radar in sonar. In a paper by Clancy et. al., the basic chirp burst waveform was modified by multiplying each chirp by a different quadratic inter-pulse code $C_n = e^{-j\pi\alpha m^2}$ where m was the chirp index and α was a user-determined parameter [3]. The effect is an apparent Doppler shift (determined by α) is applied to each successive range ambiguity. In other words, the range-folded "ghost" target returns are spread into the Doppler domain of the ambiguity function.

Simulations showed that directly applying Clancy et. al.s' method the CAS problem was infeasible. Further investigation lead to using frequency diversity to make sub-chirps unique. The expression for the SLO-CO waveform of duration T

and total bandwidth B is shown below

$$s_{SLOCO}(t) = \sum_{m=0}^{M-1} rect(\frac{t - mT_c}{T_c}) e^{j\pi\mu(t-mT_c)^2} e^{\Delta\omega(c_m-1)(t-mT_c)} \tag{4.2}$$

where M is the number of sub-chirps $T_c = T/M$ is the duration of each sub-chirp, $\mu = \frac{B}{MT_c}$ is the LFM sweep rate, and $\Delta\omega$ is a design parameter [1]. Notice the similarity between this expression and Eq. 4.1. The major difference is that instead of increasing the frequency stagger between sub-chirps by $m = 0,\ 1, \ldots,$ M-1, the frequency stagger is determined according to an integer Costas code. Non-recurrent Costas frequency coding is achieved buy choosing an integer sequence $(c_1,\ , c_2,\ \ldots,\ c_M)$ to be a circular Costas sequence of order M [1]. Costas codes and their properties are discussed in the next subsection.

A spectrogram of the SLO-CO waveform transmitted in the TREX13 experiment is shown in Fig. 4.4. The SLO-CO parameters that were used are in the figure caption.

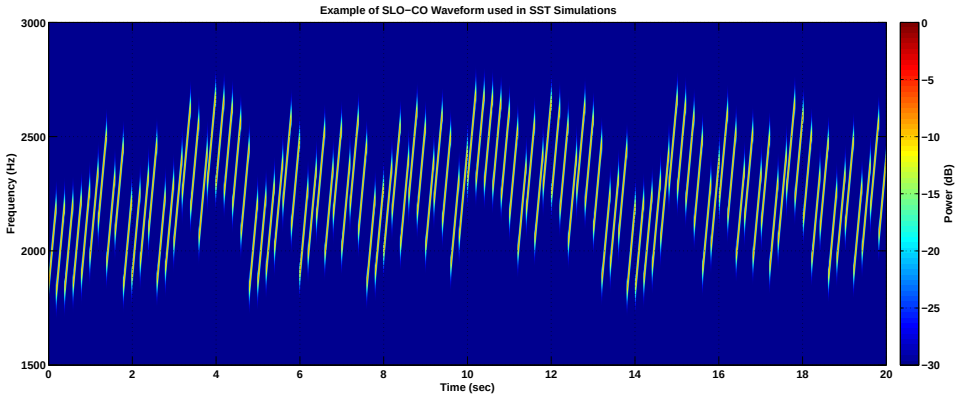

FIGURE 4.4: Spectrogram of the TREX13 SLO-CO waveform: $M = 90$, $T_c = 0.2$ sec, $\Delta f = 5$ Hz, $\mu = 2000$ Hz/sec, Overall BW = 900 Hz.

4.3.1 Costas Codes

A Costas sequence $(c_1,\ , c_2,\ \ldots,\ c_M)$ of order M is an ordered M-tuple of integers that permutes the entries of the set $1,\ \ldots,\ , M$ in such a way that $c_{i+k} - c_i \neq c_{j+k} - c_j$

whenever $1 \leqslant< j < j + k \leqslant M$ for integers i, j, and k [1]. Costas first derived the sequence in 1984 while searching for a frequency-hopped sonar waveform that had "nearly-ideal" thumbtack-like ambiguity functions [4].

Fig. 4.5 shows a frequency sequence for a circular Costas waveform with $N = 7$ and $c = (4\ ,7\ ,1\ ,6\ ,5\ ,2\ ,3)$. Assume for a moment that we are using simple pulsed sinusoids instead of the LFM chirps used in SLO-CO. The rows denote the a sub-pulse number in time, and the columns are used to denote discretized frequency. A dot indicates the frequency assigned to the associated sub-pulse. Note that each corresponding sub-pulse frequency is equal to $(c_n - 1)\Delta f$.

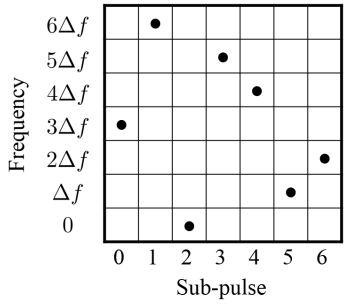

FIGURE 4.5: Example of a Costas frequency sequence, $N = 7$ and $c = (4\ ,7\ ,1\ ,6\ ,5\ ,2\ ,3)$

Costas sequences are said to be circular if applying successive circular shifts to it always results in a sequence that is itself Costas. The Welch method is known to only produce circular Costas sequences. The Welch construction method is described in detail in [14]. The concept of the circular property is demonstrated in the Fig. 4.6.

Subfigures (a), (b), (c), and (d) show examples of a copy of code being slid over itself in both the discretized time and frequency. When an overlap in time and frequency occurs, we denote this as a red dot. In Subfigure (a) we see that for this particular scenario, no pulses overlap. In Subfigures (b) and (c) we see examples where a single pulse overlaps. In Subfigure (d) we see the case where all of the pulses match. It turns out that for a circular Costas code, the number of pulses that overlap

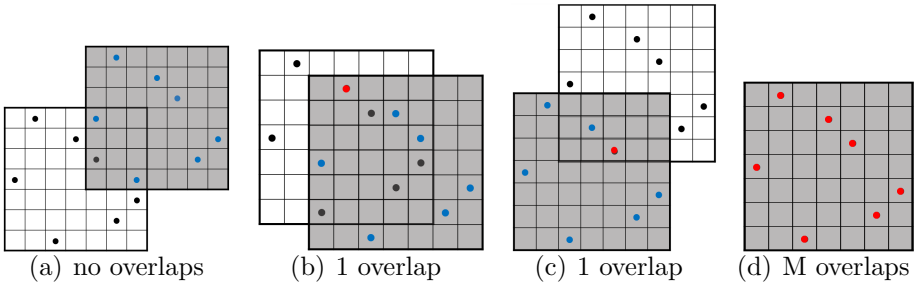

FIGURE 4.6: Example steps of the 2-D autocorrelation of a Costas frequency sequence $c = (4\ ,7\ ,1\ ,6\ ,5\ ,2\ ,3)$ to show the Costas property. (a), (b), and (c) show incomplete overlap ($\leqslant 1$ overlaps). (d) shows complete overlap (M overlaps)

is always $\leqslant 1$, except for the case where they all M of them overlap like in Subfigure (d).

This concept translates to the 2-dimensional autocorrelation of Costas waveforms. As explained earlier, the AF of a waveform is the magnitude of its 2-D autocorrelation in frequency and time. Costas waveforms nearly achieves the desirable thumbtack-like ambiguity function due to the Costas property [4]. The low sidelobes correspond to all of the $\leqslant 1$ overlaps and the tall main lobe corresponds to when all M pulses overlap which corresponds to $SLL = -20\log_{10}(M)$ dB. In the case of SLO-CO we are using LFM chirps instead of pulses which further improves the ambiguity function by enabling wideband updates with each chirp. The parameter $\Delta\omega$ for SLO-CO intuitively corresponds to the spacing between the discretized frequency space and T_c is the sub-chirp length.

4.4 Amplitude-Range-Velocity (ARV) processing

The SLO-CO waveform enables range and velocity estimates with every sub-chirp [1]. The processing method involves using a bank of M matched filters, one corresponding to each sub-chirp of the waveform and, shift them so their peaks align, and then sum their outputs. Fig. 4.7 shows the processing chain

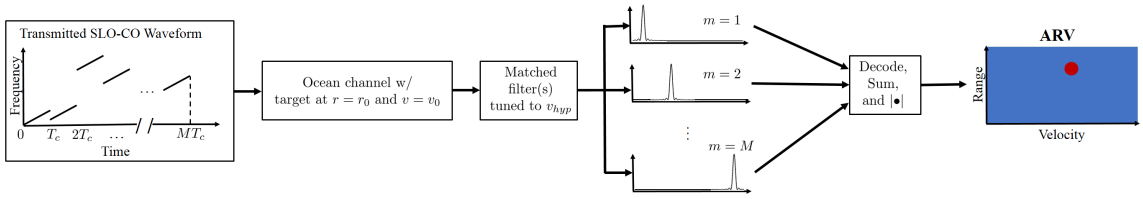

FIGURE 4.7: ARV processing chain developed for the SLO-CO waveform.

An Amplitude Range Velocity (ARV) plot is essentially a sampled version of the ambiguity function with scaled axes. ARVs are generated by applying a bank of discrete match filters, each with its own Doppler/velocity hypothesis, to a sampled received signal. The corresponding matched filter outputs are then placed in a matrix where each column represents a different velocity hypothesis and each row is the sampled matched filter output pertaining to its specific velocity hypothesis. Then the element-wise power of the matrix is plotted (usually in dB) with meaningfully scaled range and velocity axes. The rows of the resulting matrix correspond to range and the columns correspond to each velocity hypothesis. It should also be noted that ARVs are generated for a particular range and velocity window of interest.

4.4.1 Comparison of conventional CAS and SLO-CO ARVs

Section 4.2 describes conventional CAS processing (the STFT method), but the conventional CAS waveform can also be processed using ARV processing. This enables more direct comparison between the SLO-CO and CAS waveforms. ARV processing involves processing the entire conventional CAS waveform, instead of a short STFT interval. Assuming a point spread target, ARV processing the entire bandwidth of the CAS enables us to maximize range resolution and SNR gain due to pulse compression. If we look at only the zero-velocity cut across the ARV surface, the result is equivalent to conventional CAS processing with the STFT interval set to the full waveform duration.

Fig. 4.8 show side by side comparisons of ARVs for CAS and SLO-CO waveforms

whose overall BW and duration are equivalent. The CAS and SLO-CO parameters used in the example below are the same as those used in the TREX13 experiment. Color scales are also equivalent.

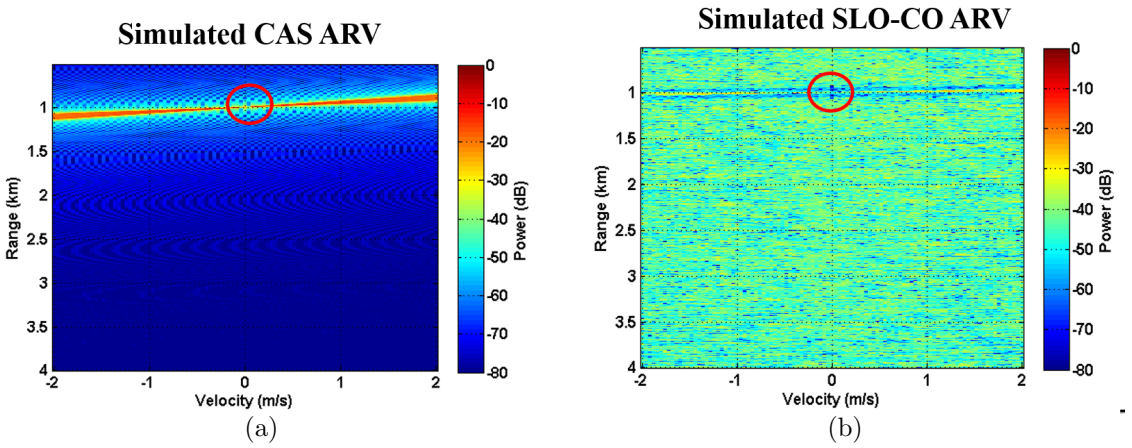

FIGURE 4.8: (Left) ARV plot of TREX13 CAS WF, $T = 18$ sec, $\mu = 50$ Hz/sec, Overall BW = 900 Hz. (Right) ARV plot of TREX13 SLO-CO WF, $M = 90$, $T_c = 0.2$ sec, $\Delta f = 5$ Hz, $\mu = 2000$ Hz/sec, Overall BW = 900 Hz.

In both plots, the target peak (0 dB) is circled in red at $v_0 = 0$ m/s and $r_0 = 1$ km. In the plot on the left we see that CAS has excellent range resolution, but relatively poor velocity resolution. The SLO-CO ARV (right) achieves the desirable thumbtack-like AF indicative of both high range and velocity resolution. The range and velocity resolution of SLO-CO is so high that it is difficult to spot the target peak given the axes scaling. It is also important to note the high update rate of these continuous active waveforms. The CAS ARV (Left) can conceivably be updated every sample by using a sliding window whereas the SLO-CO ARV (Right) is designed to be updated every sub-chirp interval (in this case 0.2 sec).

We also note that in the SLO-CO case, that achieving good resolution in both range and velocity comes at the cost of relatively high sidelobe levels ($SLL_{TREX13} \approx -20\log_{10}(90) = -39.1$ dB) that are spread in both range and velocity, whereas CAS

sidelobes decay quickly in range down to (≈ -80 dB). This behavior is intuitive when we recall the AF property that the volume under the AF surface must be conserved. So in comparison to conventional CAS, SLO-CO trades sidelobe behavior for resolution. This behavior is shown even more clearly in the target velocity cuts shown in Fig. 4.9.

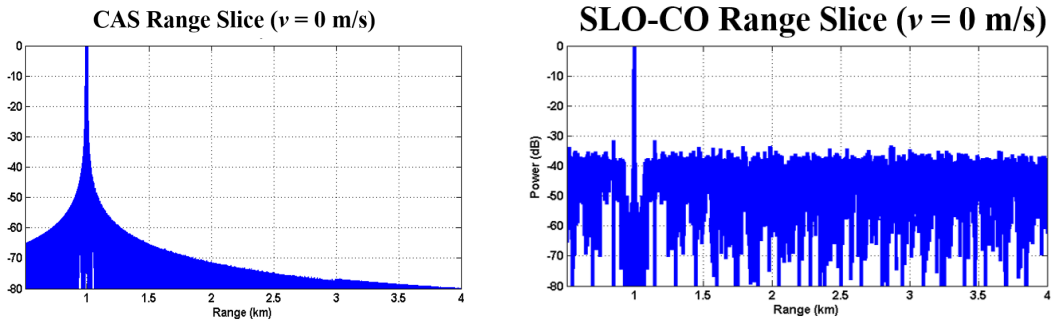

(a) (b)

FIGURE 4.9: (Left) $v_0 = 0$ m/s velocity cut of conventional TREX13 CAS ARV, (Right) $v_0 = 0$ m/s velocity cut of SLO-CO ARV.

Despite being down $\approx -20\log_{10}(M) = -40$ dB SLO-CO's sidelobes are relatively high when compared to CAS. In Chapter 6 it will be seen that the relatively high sidelobes of SLO-CO causes issues in the TREX13 experimental data.

5

Simulation Model and Simulated Results

5.1 The Sonar Simulation Toolset (SST)

The Sonar Simulation Toolset (SST) was used to evaluate the performance of the SLO-CO waveform in a realistically modeled underwater environment. The SLO-CO waveform was also tested in the Target and Reverberation Experiment 2013 (TREX13) whose results are shown in Chapter 6. The goal of using SST was to try to mimic the underwater environment expected in the TREX13 experiment to gain insight before sending the waveform to be tested in the real ocean.

SST is a tool designed to simulate an underwater acoustic environment. SST was developed at the APL-UW by Dr. Robert Goddard [15]. SST simulations are run using an object-oriented scripting language. In our case, the input to SST was sampled timeseries of SLO-CO waveforms as well as ocean environment and simulation parameters. SST allowed us to generate simulated timeseries including

1. Target echo returns with or without multi-path (reflected) returns
2. Direct blast from the source
3. Surface, bottom, and ocean volume reverberation

Despite SST's capability to generate noise, MATALB was used to add AWGN. After SST generated files containing the timeseries, MATLAB was used to read the files and perform all signal processing (e.g. summing signal components, matched filtering, etc.).

SST is structured using various component models corresponding to different parts of the ocean and sonar system [15]. Fig. 5.1 shows a high-level summary of the component model approach that was taken from [15]. These component models are explained in [15] and will not be covered in great detail in this thesis. Dr. Goddard also published a paper analyzing reverberation added by SST [16].

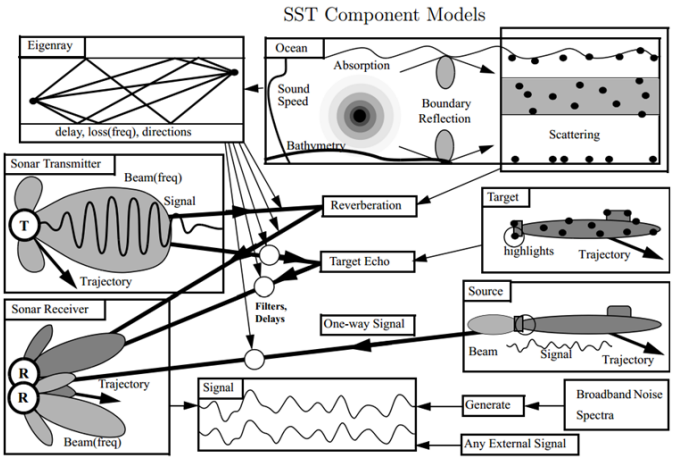

FIGURE 5.1: Figure taken from [15] showing a high-level overview of the component model structure used by SST.

5.2 SST simulations of the SLO-CO waveform

After developing an understanding about how generate simulations in SST, we generated realistic underwater simulations of the SLO-CO waveform. We started by replicating (in SST) the the MATLAB simulated results Oceans paper [1] to confirm the operation of SST. To get the results to match, it was necessary to scale the level of the reverberation generated by SST so that the Signal-to-Reverberation

Ratio (SRR) matched the SRR = 20 dB in the Oceans paper. The result is shown in Fig. 5.2. Note that these simulations assumed a single hydrophone and projector in a monostatic configuration without any direct blast signal (the direct path between the hydrophone and projector).

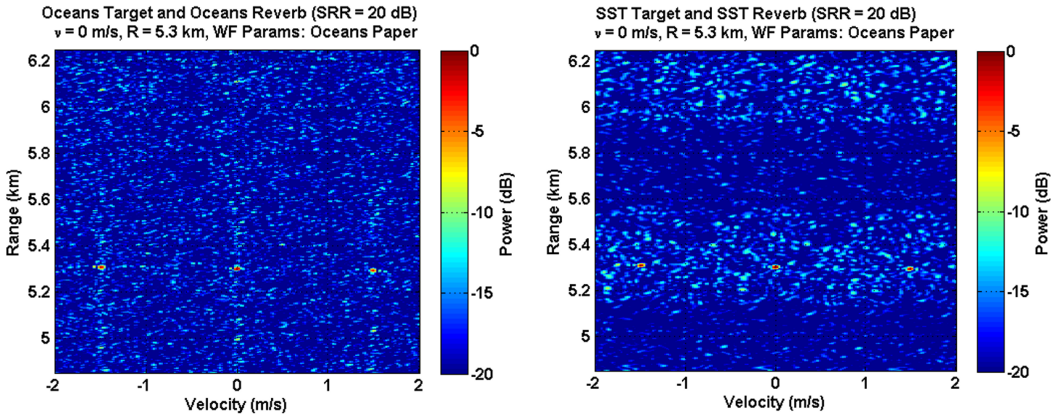

(a) Oceans paper result (b) Duplicated result using SST

FIGURE 5.2: ARVs from the Oceans paper (Left) compared to a normalized version produced by SST (Right), confirming similarity, $M = 30$, $T_c = 1$ sec, $B/M = 100$ Hz, $r_0 = 5.3$ km, $v_0 = 0$ m/s

Next attempts were made to roughly match our most recent understanding of the TREX13 experiment geometry and ocean parameters. Fig. 5.3 shows the geometry as well as the list of simulation parameters used in the proceeding simulations.

As shown in the parameter list, we used a nearly monostatic sonar and tested 3 different target positions with ground ranges (1 km, 3 km, and 5 km) corresponding slant ranges of 1.29, 3.02, and 4.95 km. Ground range is the distance between the hydrophone and the target ignoring depth and that the sonar is not perfectly monostatic. Slant ranges is the geometric distance taking all 3 dimensions into account (x, y, and depth) as well as accounting for the sonar not being perfectly monostatic.

As discussed in the beginning of Chapter 4, the direct blast from the source

directly to the receiver is a major issue when continuously transmitting the waveform. SST enabled us to look at the results with and without the direct blast included, as well as with and without the reverberation and noise included. The ARV surfaces in Fig. 5.4 show the target 1.29 km slant range cases of (a) target+noise (the noise level was set to be 30 dB at this range), (b) the target+nulled direct blast (the source level was set to be 182 dB), and (c) the target+direct blast+noise. Note that noise used was zero-mean Gaussian random noise and was applied after SST simulation.

To see the target peak, the Signal-to-Direct Blast Ratio (SDBR) was reduced by 50 dB below the SST-generated outputs. At the time, given our limited knowledge of the experimental setup, it was believed that this nulling level would reasonable. We expected there to be at least 30 dB of transmission loss between the source and array (assuming cylindrical spreading and a 1 km separation: $10\log_{10}(1000) = 30$ dB plus at least 40 dB from steering the 78 element receive array towards the target (roughly at broadside) and away from the source (roughly at endfire). Later it was determined that this was not the case. A much more in depth discussion of this issue is in Chapter 6.

Fig. 5.4 shows the ARV-processed returns progressively adding the various signal components. In (a) we see the target response + noise at $r_0 = 1.3$ km and $v_0 = 0$ m/s. (b) shows the ARV of target + direct blast, while (c) shows the ARV of the target + reverb + direct blast + noise components. Also note in (b) and (c), we see the direct blast coming from the source in the ARV at (0 m/s, 0.673 km) which corresponds to half of the one-way distance between the receiver and the source of 1.346 km. We also note that the trail of returns coming from the direct blast and target. These are due to the realistically simulated multi-path reflections.

Fig. 5.5 shows results from the target+direct blast+noise returns from SST for all three slant ranges (1.29, 3.02, and 4.95 km). Sub-figures (a), (c), and (e) show the ARVs while sub-figures (b), (d), and (f) show the respective matched filter outputs

(target velocity slices). Note that plot (a) in Fig. 5.5 is a repeat of (c) from Fig. 5.4. The plots were grouped in this way to show the diminishing response as the target moves out in range. Also note that the discrepancy in the nominal dB levels between the ARVs and their corresponding matched filter outputs is due to normalization. The relative levels are what are of importance.

In these results, the Signal-to-Reverberation Ratio (SRRs) were scaled so that the target would disappear as it approached 5 km. It is also interesting to note how in the title of each of the plots, the SNR is listed to decrease from 30 dB to 19 dB to 13 dB as the target moves out in rage. The decrease in SNR is due to the increasing amount of realistically-modeled transmission loss of the echo return as the target moves out in range.

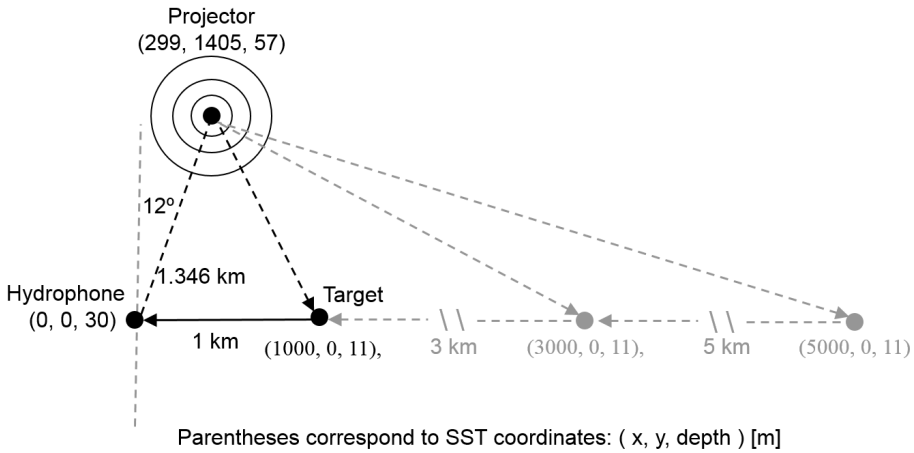

(a)

Ocean Parameters:
- Ocean Depth: 60 m
- Bottom Type: MediumSand
- Wind Speed: 0.1 m/s

Eigenray Parameters:
- Max Eigenrays Tested: { 32, 64, 72 }
- Max Sur Bounces: { 8, 16, 18 }
- Max Bot Bounces: { 8, 16, 18 }
- Max 2-way Sur Bounces: { 8, 16, 18 }
- Max 2-way Sur Bounces: { 8, 16, 18 }

Reverb Parameters:
- Surface Type: APL Surface
  (only input parameter is wind speed)
- Volume Scattering Strength = -90 dB
  (from Burdic book)
- Bottom Type: Jackson Bottom
  (only input parameter is bottom type)

Target Parameters:
- Target Positions:
  { (1000, 0, 11), (3000, 0, 11), (5000, 0, 11) }
- Target Velocity: 0 m/s
- Target Type: Point
- Target Strength: 0 dB

Waveform Parameters:
- Source Level: 182 dB
- Number of Pulses: 100
- PRI: 0.2 sec
- CPI: 20 sec
- F_0: 1800 Hz
- Chirp BW: 400 Hz
- Fs: 4495 Hz

Sonar Parameters:
- Projector Position: (299, 1405, 57)
- Projector Directivity: ITC-2015
- Hydrophone Beam Pattern: 15° Cone
- Hydrophone Position: (0, 0, 30)

Brackets correspond to target ranges: { 1, 3, 5 } [km]
Parentheses correspond to SST coordinates: (x, y, depth) [m]

(b)

FIGURE 5.3: (top) Experimental geometry used in SST simulations with target ground ranges of 1, 3, and 5 km. (bottom) List of parameters used in the SST simulation.

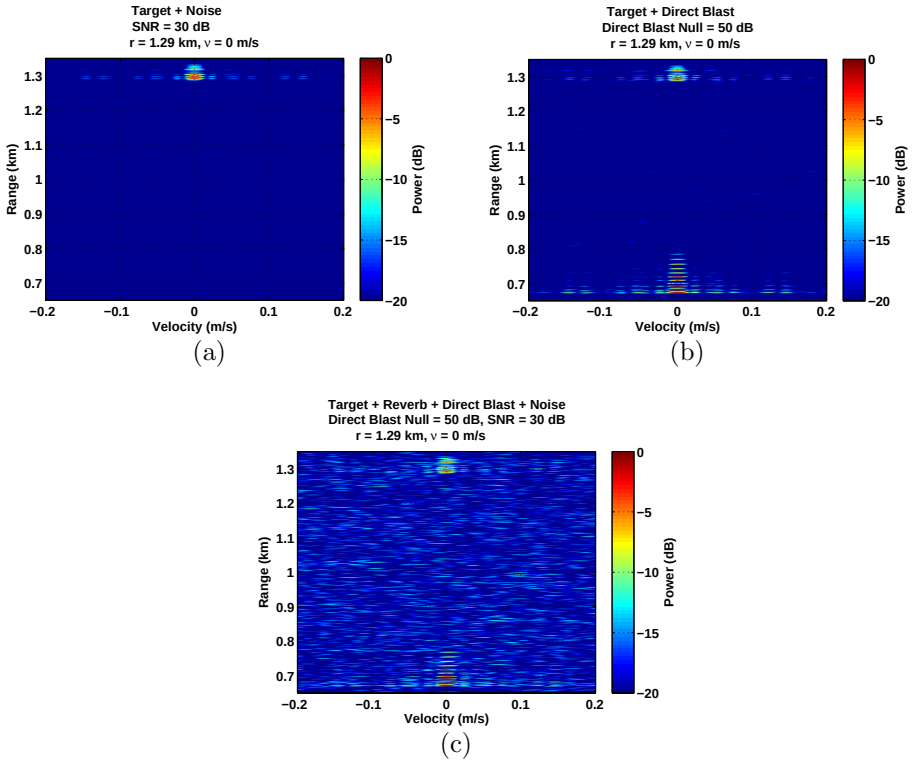

FIGURE 5.4: ARVs produced from timeseries generated by SST for the 1.29 km slant range geometry (a) target + noise, (b) target + direct blast (c) target + reverb + direct blast + noise, Simulation parameters are shown in Fig. 5.3.

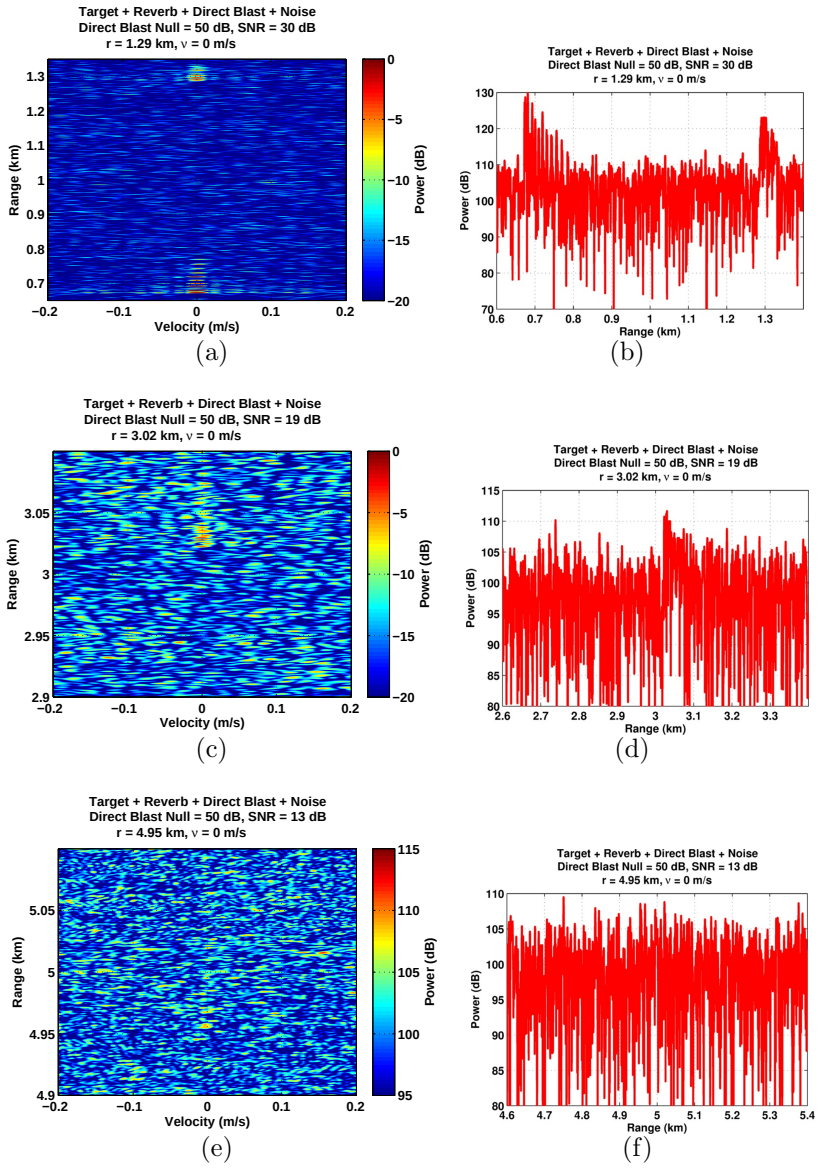

FIGURE 5.5: (a), (c), and (e) show ARVs produced from SST timeseries of the 1.29, 3.02, and 4.95 km target slant range cases for target + reverb + direct blast + noise using simulation parameters shown in Fig. 5.3. (b), (d), (f) show the zero velocity cuts from their respective ARVs

6

Target and Reverberation Experiment 2013 (TREX13) Results

The Target and Reverberation Experiment 2013 (TREX13) was performed May 14, 2013 in the Golf of Mexico near Panama Beach, Florida. A number of CAS waveforms were tested, including conventional CAS as well as the SLO-CO waveform. The geometry was nearly monostatic with an ITC-2015 acoustic transducer placed at endfire approximately with 50 m from the 78 hydrophone triplet Five Octave Research Array (FORA) [17]. For each waveform trial, the waveform was transmitted continuously as an echo repeater was towed radially away from the array and transducer to approximately 10 km over the span of about an hour.

The data available for us to process at Duke consisted of array element-level data as well as beam-level data which was beamformed by the experimenters. The experimenters used 48 of the 78 triplets to generate 157 beams. Beam 101 was steered in the direction of the echo repeater during both the SLO-CO and CAS trials. Between each consecutive 18 second waveform transmission, there was a two second gap. The CAS and SLO-CO parameters used can be found in the caption of

Fig. 4.8.

Given that the array was placed only ≈ 50 m from the continuously transmitting source, it is intuitive that the dominant component of the received signal was the direct blast (direct path from source to receiver). Fig. 6.2 shows plots of the relative levels of the element and beam-level signals for both conventional CAS and SLO-CO trials. We also see that the beamformer nulls the direct blast by ≈ 35 dB for both the CAS and SLO-CO trials. This is because the target beam (red) is steered roughly towards broadside which nulls the source direction (endfire).

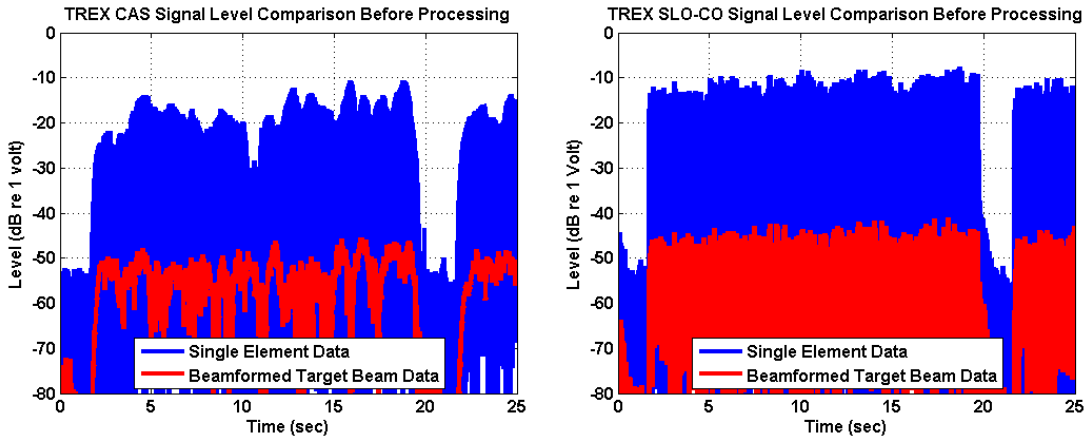

(a) (b)

FIGURE 6.1: Signal level plots comparison of element-level and beamformed of CAS and SLO-CO waveforms from TREX13 experiment. (a) CAS, (b) SLO-CO

Example spectrograms of the target beam data are shown in Fig. 6.2. Again the dominating component is the direct blast. Observe that both signals are present in the same band (1.8 to 2.7 kHz). The signal distortion for both CAS and SLO-CO is due is due to both the beamformer and propagation effects due to the real ocean channel. The light blue "trailing" in time, especially present in the CAS spectrogram, is due to reverberation and multi-path in the channel. The vertical streaks in the SLO-CO spectrogram are caused by the abrupt discontinuities in frequency caused by the Costas frequency-staggering.

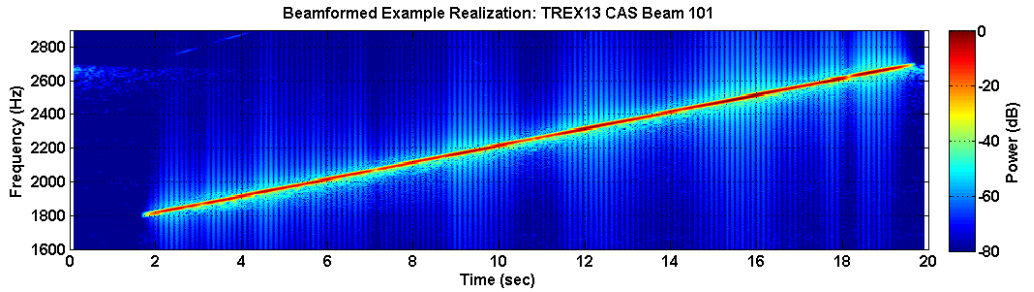

(a)

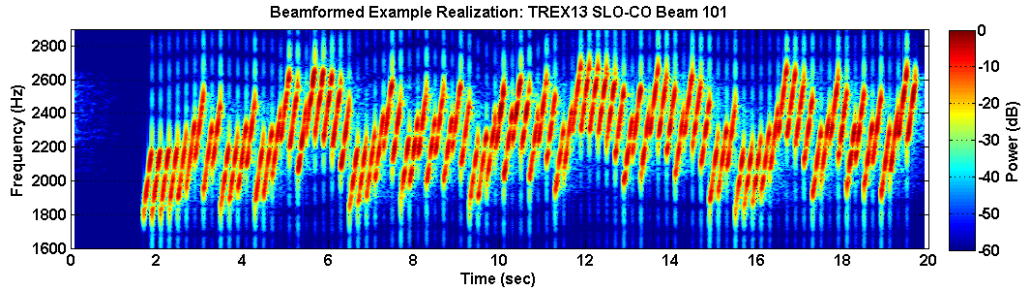

(b)

FIGURE 6.2: Example spectrograms of single beamformed realizations of CAS and SLO-CO waveforms. (a) CAS, (b) SLO-CO

6.1 Conventional CAS result

Conventional CAS processing (explained in Section 4.2) was performed on first 30 minutes of the beamformed CAS data. The resulting range vs. time plot is shown in Fig. 6.3. The processing parameters used to generate the plot are included in its title.

At the $r = 0$ km over the entire thirty minutes we see the red (0 dB) streak which is the direct blast from the transducer to the array. The trailing yellow into light blue from zero to roughly one kilometer are the range sidelobes of the direct blast. The echo repeater target and boat towing it are indicated by the light blue diagonal lines that moves outward in range and start to disappear at roughly 3 km. Note that the echo repeater was set up in to re-transmit the received waveform every alternating realization. Looking closely, this behavior is indicated by the target disappearing

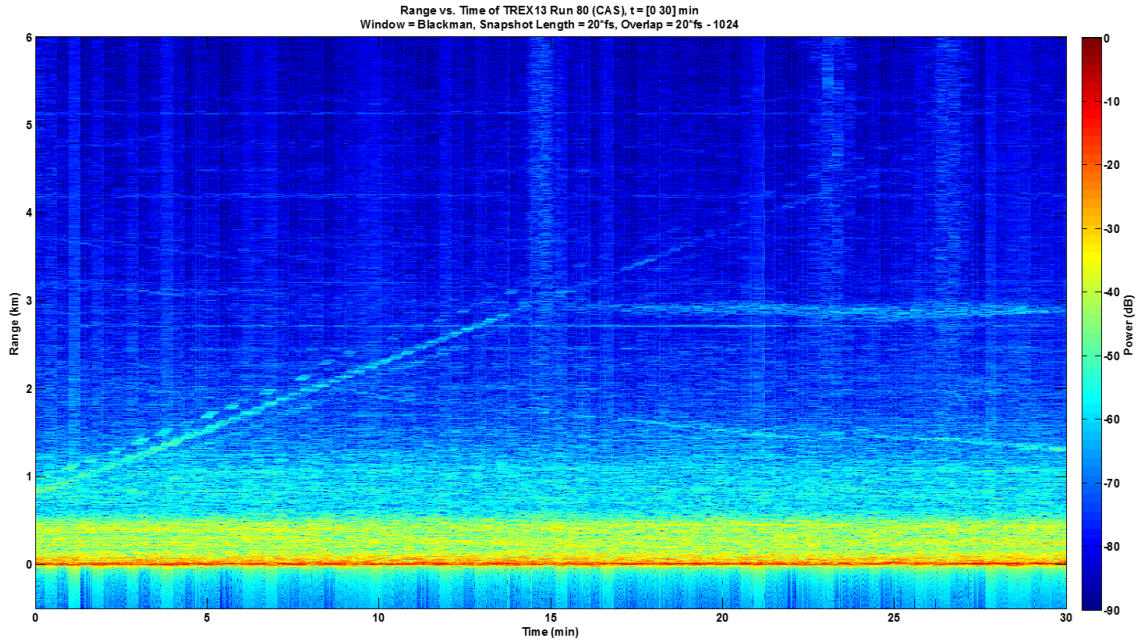

FIGURE 6.3: Conventional CAS Range vs. Time: First 30 minutes

and reappearing throughout the track.

6.2 The TREX13 SLO-CO direct blast sidelobe level issue

Processing the experimental SLO-CO data yielded some informative results. This section is dedicated to explaining why the direct blast sidelobes masked the target, as well walking through a rough computation of how much direct blast suppression would be necessary to uncover the target. The proceeding section explains the ongoing attempts at overcoming the issue.

ARV processing, explained in Section 4.4, was applied to both the beamformed CAS and SLO-CO data. ARV-processed example realizations are shown in Fig. 6.4. The CAS realization is on the left and the SLO-CO realization is on the right. Note that there is a good match between the simulated ARVs (no reverb or noise) from Section 4.4.1 and the experimental data shown below, at least for the dominating direct blast component.

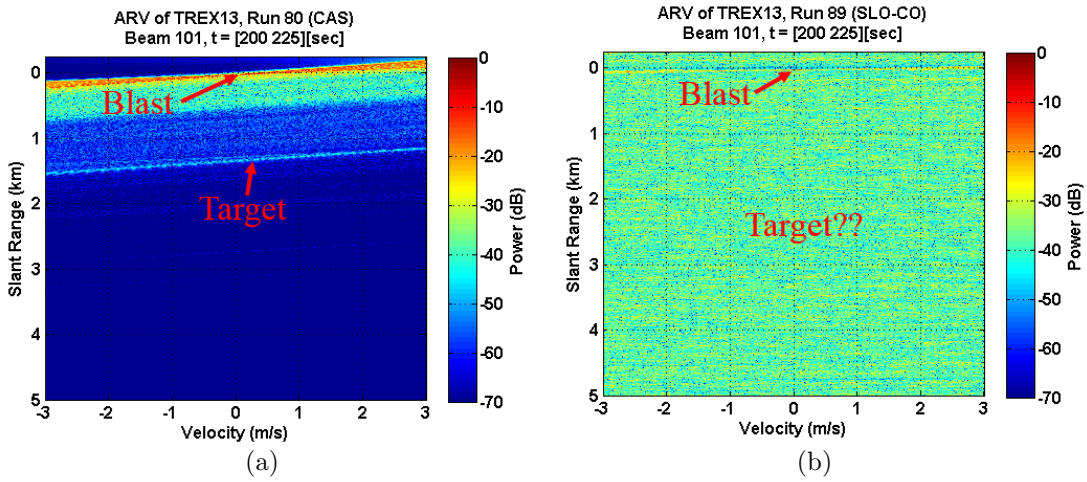

FIGURE 6.4: Example TREX13 target beam ARVs: (a) CAS and (b) SLOCO

In the CAS ARV (left) we observe the loud (0 dB) direct blast at $(r, v) = (0 \text{ km}, 0 \text{ m/s})$ as well the echo repeater target indicated by the blue streak (-40.2 dB) at $r = 0.5$ km. In the SLO-CO ARV (right) we also immediately spot the loud (0 dB) direct blast at $(r, v) = (0 \text{ km}, 0 \text{ m/s})$, but are unable to spot the target. A 2-D peak-finder was also applied to various SLO-CO realizations but we still were unable to find a target peak that corresponded to the ground truth GPS data. It was eventually determined that the target was masked by the ≈ -33.4 dB sidelobe background due to the direct blast. The relative levels can be seen even more clearly in element-level matched filter outputs shown in Fig. 6.5.

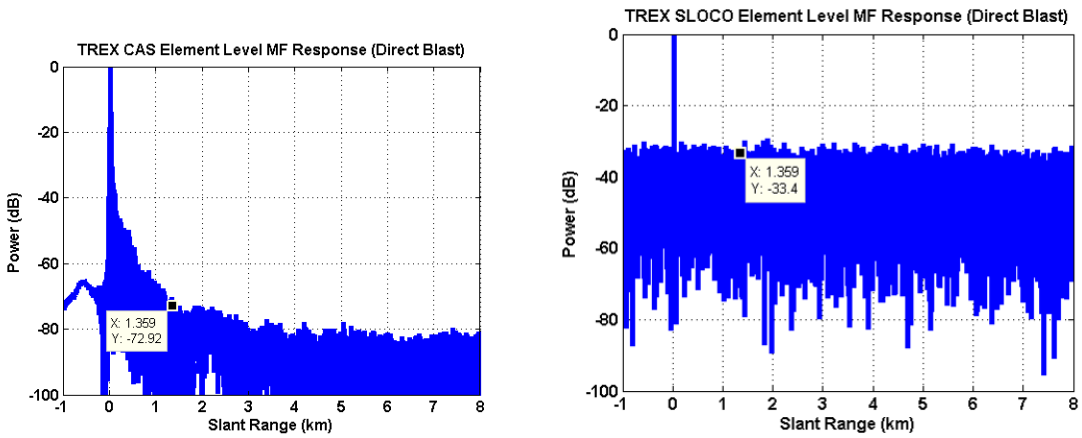

(a) (b)

FIGURE 6.5: Matched filter outputs of element level data: (a) CAS and (b) SLOCO

The plots in Fig. 6.5 enable a clear comparison of the range sidelobes of the direct blast for CAS and SLO-CO. The CAS (left) range sidelobes rapidly decay away from the direct blast peak. The SLO-CO (right) range sidelobes remain are relatively flat over all ranges of interest. Note that the same beamformed data also exhibits these same sidelobe behaviors. In both cases shown the ground truth range of the masked target is $r_0 = 1.359$ km. The direct blast sidelobe level at the range of the masked target is indicated by the black marker. For CAS, the Sidelobe Level (SLL) at the point of the target is $SLL_{\text{CAS}} = -72.9$ dB, while for SLO-CO $SLL_{\text{SLO-CO}} = -33.4$ dB making $SLL_{\text{SLO-CO}} - SLL_{\text{CAS}} = 39.54$ dB.

Keeping these range sidelobe levels in mind, we investigate the beamformed data. The CAS bearing vs. slant range plot is shown in Fig. 6.6 (left) which is generated by match filtering each individual beam. The plot on the right is a replica of the one on the left, except zoomed in around the direct blast range ($r_{\text{blast}} = 25$ m). We see the circled -74.3 dB target at $(\cos(115.8^\circ), r_0) = (-0.44, 1.36 \text{ km})$. The direct blast level in the target beam is -34.1 dB and is indicated by the black marker in the plot on the right. Because the 0 dB reference is the direct blast peak at endfire, it

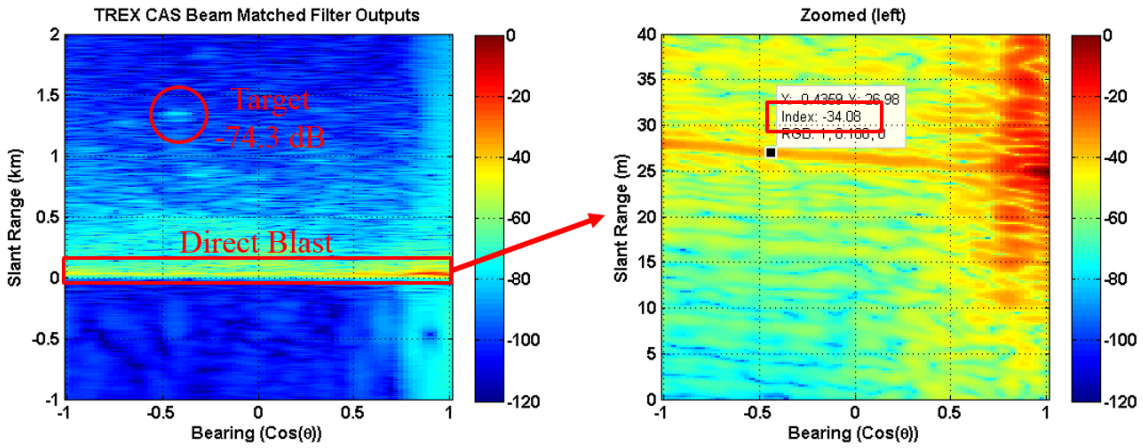

FIGURE 6.6: TREX13 conventional CAS trial beamformed and match filtered indicating the level of direct blast nulling due to the array

is intuitive that -34.1 dB is the amount of direct blast nulling due to the array. The direct blast nulling due to the array, along with the relatively low range sidelobes of CAS is what enables us to visually pick out target peak.

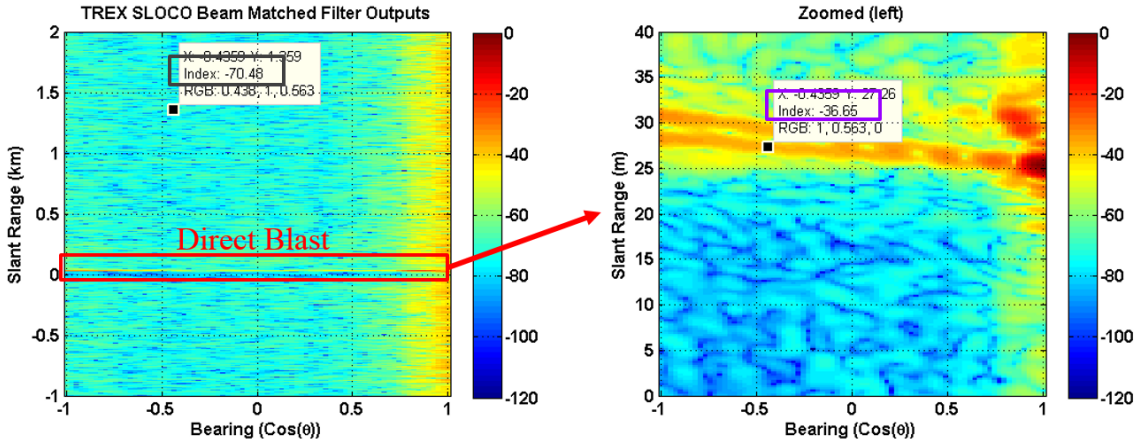

FIGURE 6.7: TREX13 SLO-CO trial beamformed and match filtered indicating the level of direct blast nulling due to the array

The same bearing vs. slant range plots, but for a SLO-CO trial, are shown in Fig. 6.7. In the plot on the right, we see that the direct blast nulling due to the array for SLO-CO is roughly -36.7 dB. Because the same beamformer was used for

both SLO-CO and CAS, we can confirm that this roughly matches the -34.1 dB blast nulling for CAS. The marker in the plot on the left indicates the -70.5 dB sidelobe level after beamforming that masks the target. We we confirm this level by recalling from the element-level data was $SLL_{\text{SLO-CO}} = -33.4$ dB and taking

$$SLL_{\text{SLO-CO}} + \text{SLO-CO blast array nulling} = -33.4 - (-36.7) = -70.1 \text{ dB} \quad (6.1)$$

amounts to a difference of only 0.4 dB and confirms the post-beamforming sidelobe level that masks the target.

Now we can finally predict the masked SLO-CO target level as well as minimum level of additional nulling that would be necessary to uncover the target. The matched filter responses for CAS and SLO-CO target beam signals which are essentially cuts across the plots in Fig. 6.7 at the target beam bearing are shown in Fig. 6.8. The annotations in the plots help to illustrate the computation.

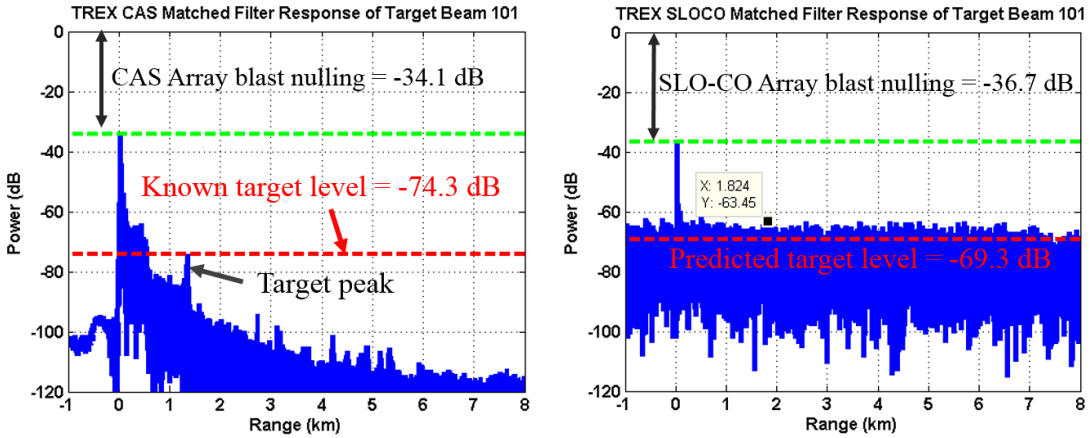

FIGURE 6.8: Comparison of TREX13 conventional CAS and SLO-CO trials beamformed and match filtered. Annotations indicate how the predicted SLO-CO target level is computed.

In an experimental log with the TREX13 dataset, a note was made that the echo repeater target was set up to repeat the CAS signal at a level of 0 dB (no gain) and

the SLO-CO signal at a level of +5 dB (5 dB gain). Taking this into account and assuming that the nominal target level for both CAS and SLO-CO are roughly the same (-74.3 dB), we predict that the masked SLO-CO target level is

$$\text{Predicted masked SLO-CO target level} = -74.3 + 5 = \underline{-69.3 \text{ dB}} \tag{6.2}$$

Taking the difference between this and the post-beamforming direct blast sidelobe level of -69.3 dB, we predict the minimal level of additional direct blast suppression that would be necessary to uncover the target to be

$$\text{Additional blast SL blast nulling} = -69.3 - (-63.5) = \underline{-5.8 \text{ dB}} \tag{6.3}$$

Note that this estimation is really only a rough baseline. In reality, the true level may be highly dependent on varying ocean characteristics, the difference response of the beamformer to conventional CAS and SLO-CO waveforms, etc.

There are a number of ways that the SLO-CO sidelobes due to the direct blast could theoretically be mitigated to uncover the target. Two methods that were tested involve adaptively suppressing the direct blast as well as determining a revised SLO-CO parameter set with lower sidelobes. The next two sections highlight these attempts.

6.3 Attempts at recovering SLO-CO experimental results

6.3.1 Adaptive filtering

One attempt at mitigating the direct blast involved the use of an adaptive filter to suppress the direct blast component from the target beam. A time-domain Wiener filter was used to determine $\hat{b}[n]$, the Minimum Mean Square Error (MMSE) estimate of the direct blast in the target beam. Next the estimated direct blast was subtracted from the target beam. A block diagram of the filter is shown in Fig. 6.9.

A detailed derivation for for the tap-weight matrix formulation of the Wiener filter is available in Kay's "Statistical Signal Processing: Volume I" [9] and more

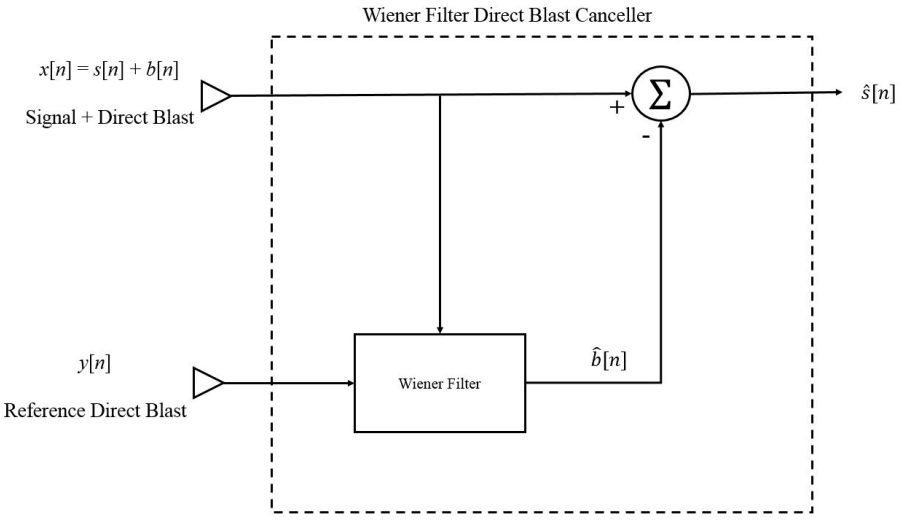

FIGURE 6.9: Schematic diagram of adaptive direct blast canceler utilizing the Wiener filter.

general information on Wiener filtering is available in Haykin's book on adaptive filter theory [18]. From Kay's derivation, the tap weight matrix becomes

$$\boldsymbol{W} = \boldsymbol{R}_{\boldsymbol{xy}}\boldsymbol{R}_{\boldsymbol{yy}}^{-1} \tag{6.4}$$

where $\boldsymbol{R}_{\boldsymbol{yy}} = \mathbb{E}\{\boldsymbol{y}\boldsymbol{y}^H\}$ and $\boldsymbol{R}_{\boldsymbol{xy}} = \mathbb{E}\{\boldsymbol{x}\boldsymbol{y}^H\}$. The expected auto and cross-covariance matrices are unavailable, so we plug in the estimates $\hat{\boldsymbol{R}}_{\boldsymbol{yy}} = \frac{1}{N}\sum_{n=1}^{N}\boldsymbol{y}_n\boldsymbol{y}_n^H$ and $\hat{\boldsymbol{R}}_{\boldsymbol{xy}} = \frac{1}{N}\sum_{n=1}^{N}\boldsymbol{x}_n\boldsymbol{y}_n^H$. The timeseries $x[n]$ was chosen as beam 101 (steered in the target direction), while $y[n]$ was chosen to be the endfire beam (steered in the direction of the source). The diagram below depicts an example of how $\boldsymbol{x}_n$ and $\boldsymbol{y}_n$ were formed using blocks of data. The example shows the case where the current vector being estimated is $\hat{\boldsymbol{b}}_3$. The example uses $M = 3$ taps, $N = 5$ snapshots, and $O = 1$ which is the number of overlapping samples between consecutive snapshots.

Plugging these into Eq. 6.4 this allows us to compute a block of the target return estimate without the direct blast.

$$\hat{\boldsymbol{s}}' = \boldsymbol{x}' - \boldsymbol{W}\boldsymbol{y}' \tag{6.5}$$

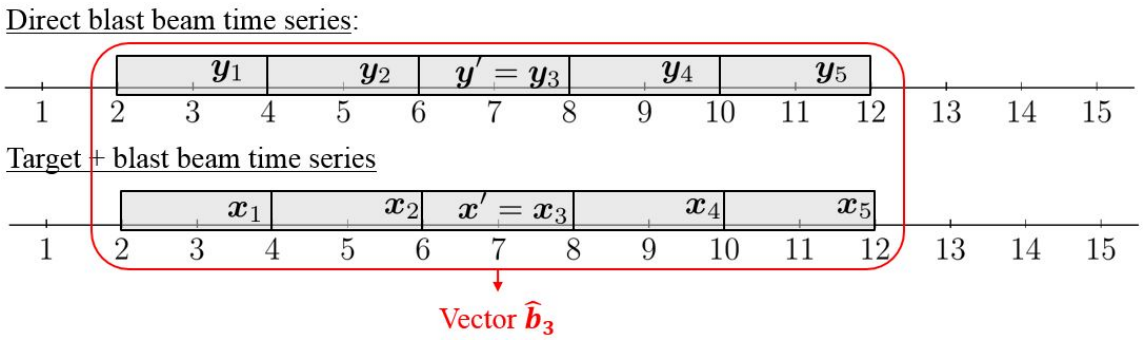

FIGURE 6.10: Diagram showing how snapshots were developed for block weight matrix Wiener filter implementation.

This processing was repeated until the entire $\hat{s}[n]$ was estimated. The resulting $\hat{s}[n]$ was then processed using the previously explained methods (ARV and conventional CAS processing).

Various values of M, N, and O were tested on both the CAS and SLO-CO data. The best result for CAS was when $M = 2$, $N = 5$, and $O = 0$. The conventional CAS processing result for $M = 2$ is shown on the right in the Fig. 6.11. The result without the direct blast canceler is shown on the left for comparison.

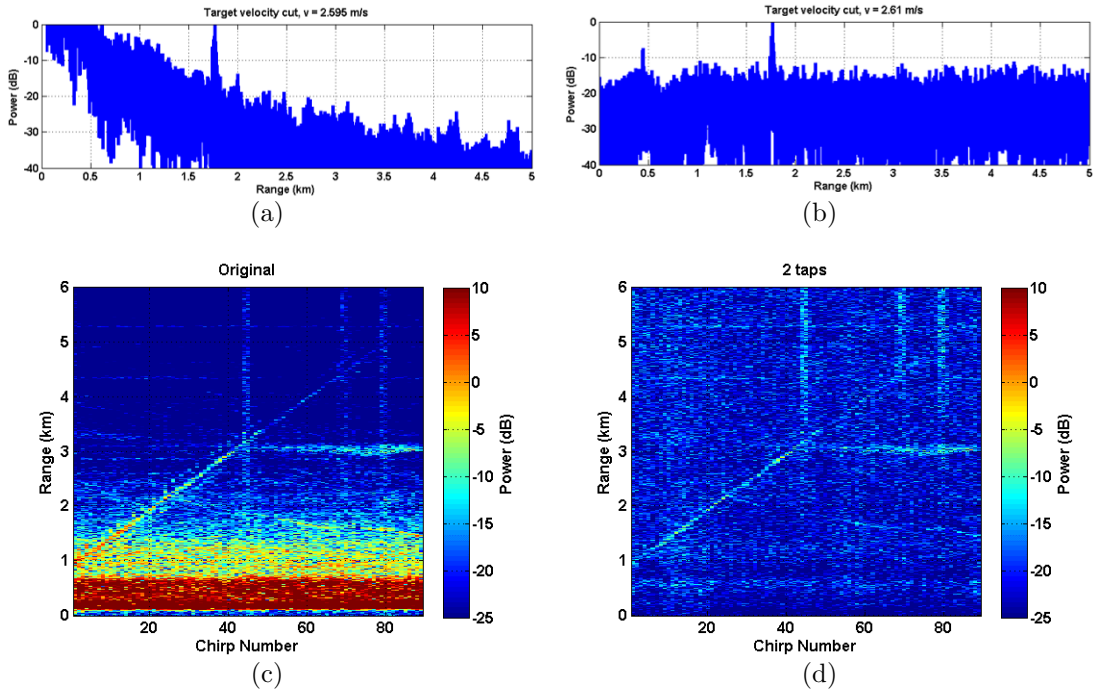

FIGURE 6.11: (left) TREX13 conventional CAS result without direct blast cancellation (right) TREX13 conventional CAS result with direct blast cancellation

The conventional CAS results without direct blast suppression are shown on the left in Fig. 6.11. The direct blast is represented by the high level returns (red streak in (c)) from approximately 0 to 0.75 km and its sidelobes are represented by mid level returns (yellow in (c)) from approximately 0.75 to 1.25 km. The target track is represented by the light blue diagonal line. The figures on the right of Fig. 6.11 are results with direct blast suppression applied. We see that the direct blast as well as its sidelobes are no longer present in (d) and the target return remains intact. Plots (a) and (b) show an example cut across the (c) and (d) respectively clearly show the levels before and after direct blast suppression.

The same adaptive filtering implementation was was applied to the SLO-CO data prior to ARV processing, but without success. The lack of success is hypothesized to be due to (1) the rapid jumps in frequency of the SLO-CO when compared to CAS

or (2) the high level of spectral overlap between the direct blast and delayed target signal. These two factors would result in making it for the adaptive filter to adapt to the direct blast signal without corrupting the target signal. Work on this adaptive filtering problem is ongoing.

6.3.2 Waveform re-design

Another promising method of reducing the SLO-CO direct blast issue involves simply varying SLO-CO parameters to reduce the background sidelobe level.

Costas code length M

Increasing the Costas code length M is an initial intuitive method for reducing the sidelobe level. The plot in Fig. 6.12 (a) shows the approximate SLO-CO SLL for various values of M.

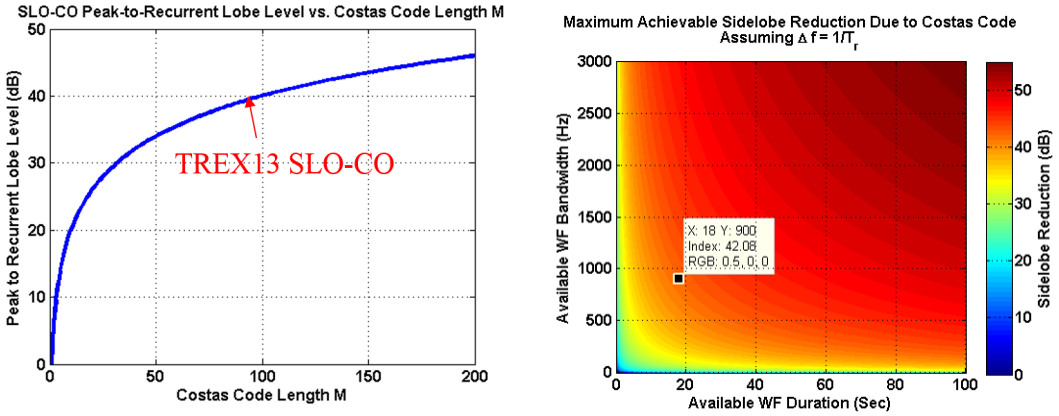

(a) (b)

FIGURE 6.12: (left) SLO-CO SLL vs. Costas code length M (right) Maximum Achievable SLO-CO SLL reduction due to Costas coding as a function of available waveform bandwidth and duration.

Notice that the y-axis of Fig. 6.12 (a) refers to the "Peak to Recurrent Lobe Level." This is level is equal to the SLL in the case where $\Delta f = 1/T_P$. This is due to the property of the Costas code that sets the SLL to be $20\log_{10}(M)$ down

from the target peak. Fig. 6.12 (a) indicates the issue that additional SLL reduction diminishes logarithmically as a function of M. For example increasing $M = 90$ by a factor of two to $M = 180$ in the TREX13 experiment would result in only a 6 dB improvement. Fig. 6.12 (b) shows the maximum achievable SLL reduction (- minimum SLL) due to the Costas code as a function of the total BW and and total waveform duration under the assumption that $\Delta f = 1/T_r$. The black marker corresponds to the TREX13 design constraints. Therefore the effective reduction in SLL due to increasing M diminishes quickly and M is also bounded by the design constraints on waveform duration and bandwidth.

Reducing sub-chirp bandwidth overlap

Given the issues and constraints on increasing M, other methods to decrease the SLO-CO SLL beyond $-20\log_{10}(M)$ were investigated. The alternative that was found involves reducing the overlapping bandwidth between sub-chirps. This involves both increasing the amount of frequency stagger Δf beyond $1/T_r$ as well as reducing the sub-chirp LFM sweep rate μ.

There was $\approx 99\%$ sub-chirp BW overlap in the SLO-CO waveform used in the TREX13 experiment. Therefore the SLL was dictated almost entirely by the Costas code length $M = 90$. To investigate the trade-offs involved with decreasing the sub-chirp BW overlap, a number of simulations were performed. Spectrograms of three different waveforms with varying levels of sub-chirp BW overlap are shown in Fig. 6.13.

As seen in Fig. 6.13 (a-c), the sub-chirp BW overlap was set to $\{50, 10, 0\}$ % by setting the LFM sweep rate $\mu = \{90, 50, 0\}$ Hz/sec, respectively. In all three plots, $M = 30$, $T_r = 0.667$ and $\Delta f = 20/T_r$ were fixed parameters. Each of these waveforms were designed to fall within the design constraints of the TREX13 experiment. Their corresponding ARVs and target velocity cuts are showin in Fig. 6.14.

Observing the various target velocity cuts in Fig. 6.14, it is recognized that reducing sub-chirp BW overlap reduces the SLL (at least at low velocities) to far beyond -29.6 dB due to the $M = 30$ Costas code. The 10% and 0% overlap cases also successfully achieve a lower SLL than the original TREX13 submission (≈ -39.1 dB). The ARV surfaces show how this SLL reduction comes at the cost of resolution.

Another undesirable effect caused by increasing δf beyond $1/T_c$ are the appearance of "range grating lobes" which are discussed in detail by Levanon [5]. Range grating lobes are essentially sub-peaks whose resolution correspond to the entire waveform BW. These sub-peaks grouped together form the overall target return peak whose resolution corresponds to the BW of an individual sub-chirp.

Re-designed SLO-CO for TREX13

If a new SLO-CO waveform could be re-designed for the TREX13 experimental setup, the following parameters would be used: $M = 30$, $T_r = 0.6$ sec, $f_0 = 1800$ Hz, $\mu = 30$ Hz/sec, and $\Delta f = 20/T_r$. Additionally we would apply a Blackman window to each of the transmitted sub-chirps to mitigate the sidelobes resulting from each individual sub-chirp. The ARV range and velocity cuts with the revised parameter set is shown in Fig. 6.15

As seen in the plots in Fig. 6.15, the SLL in the velocity region of interest ($-5 \leqslant v \leqslant +5$ m/s) is dropped -70 dB, which is comparable to the conventional CAS SLL. This is due to the reduced overlapping sub-chirp bandwidth in addition to the Blackman window applied to sub-chirps. This much lower SLL could easily mitigate the previous issues with the direct blast.

Additionally, this SLO-CO parameter set causes an ambiguity-free velocity region to appear in the ARV. The sub-peaks or "picket fence" bordering this region is due to the cross-ambiguity of the various sub-chirps. In an experiment, the level of the "picket fence" returns of the direct blast would likely be high, however since the

source is not moving relative to the array, these returns remain stationary. Given the relatively slow speed that boats and submarines travel, it is expected that most moving target responses will appear in this ambiguity free region and would not be obstructed by the direct blast.

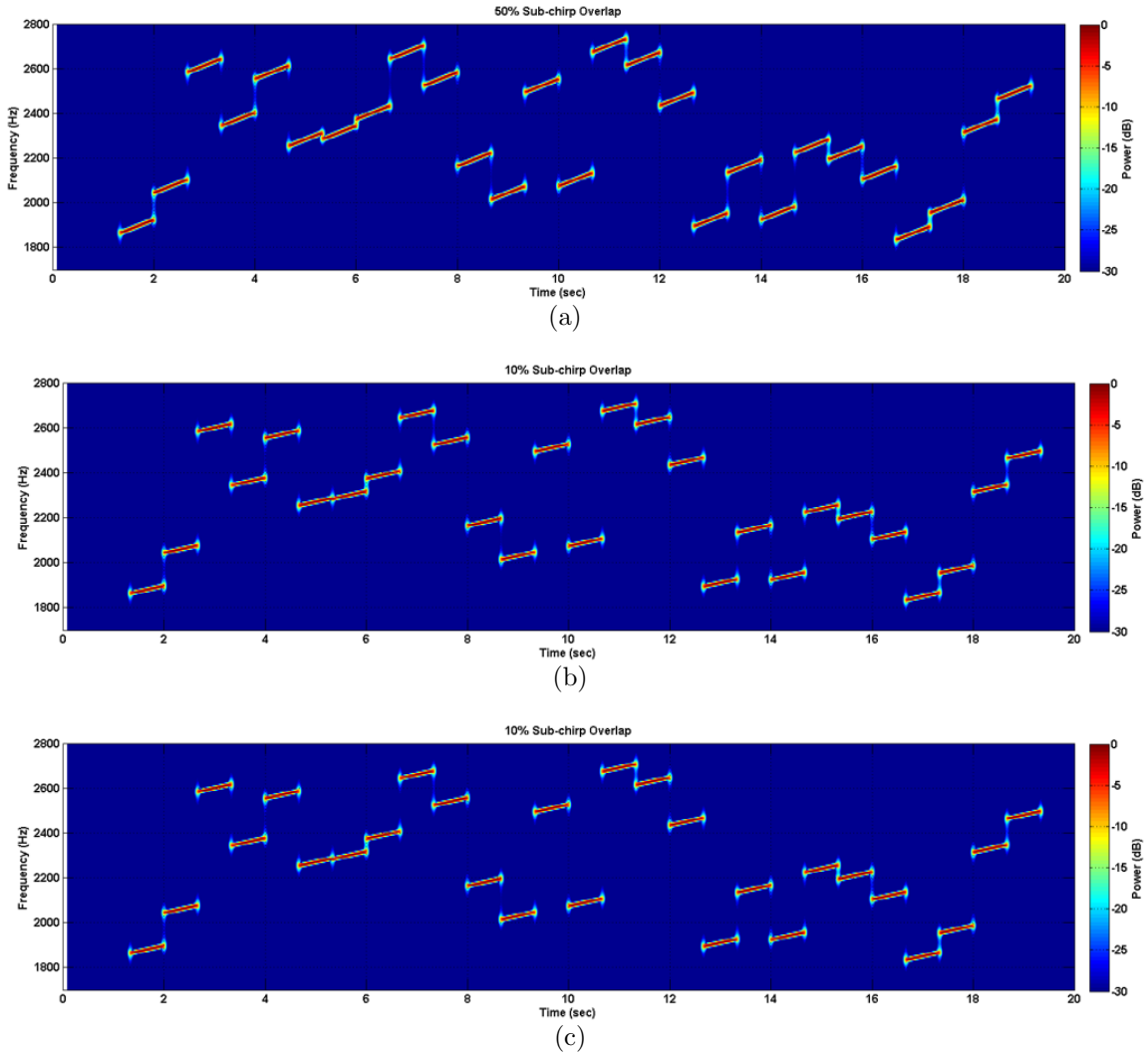

FIGURE 6.13: SLO-CO spectrograms with sub-chirp BW overlap $\{50, 10, 0\}$ % corresponding to (top), (middle), and (bottom). In all three, $M = 30$, $T_r = 0.667$ and $\Delta f = 20/T_r$ are fixed.

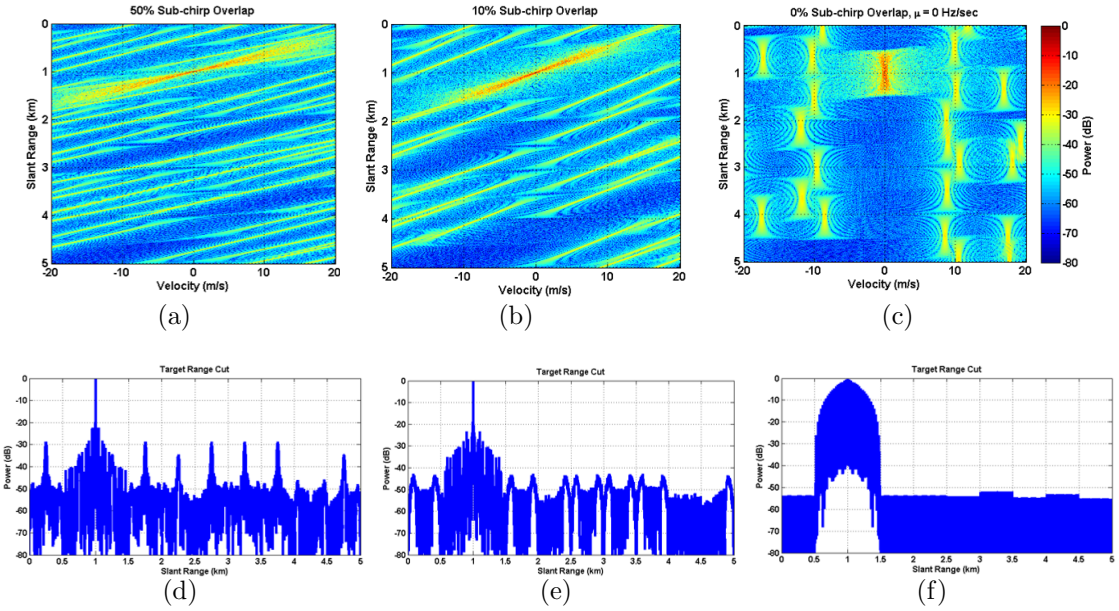

FIGURE 6.14: (a), (b), and (c) are SLO-CO ARVs and (d), (e), and (f) are SLO-CO matched filter outputs with varying sub-chirp BW overlap corresponding to the waveforms in Fig. 6.13.

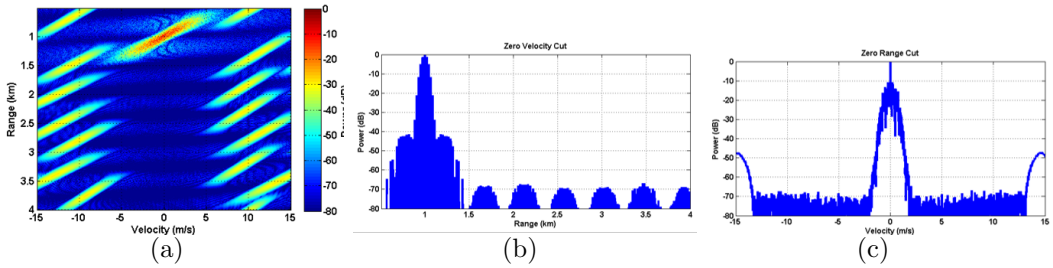

FIGURE 6.15: (a) ARV, (b) target velocity cut, and (c) target velocity cut using newly recommended SLO-CO parameters if there were another experiment similar to TREX13.

7

Conclusions

This thesis introduces the topic of waveform design for the Continuous Active Sonar (CAS) application as well as presenting the Slow-Time Costas-Coded (SLO-CO) CAS waveform. The SLO-CO waveform shows promise for delivering high range and velocity revisit rates and wideband processing gains while suppressing range ambiguities. TREX13 experimental results reveal that SLO-CO's relatively high direct blast sidelobes cause the target to be masked. Adaptive direct blast cancellation and re-designing the waveform were discussed methods of mitigating the direct blast issue.

Future work involves performing more SST simulations of the SLO-CO waveform in with various experimental geometries and ocean environments. Performing these simulations with the foresight acquired from the mistakes made with the TREX13 submission could definitely be informative. Doing so could hopefully enable us to determine a set of SLO-CO design rules for each environment that ensures that the direct blast will not cause issues.

Other future work includes looking deeper into direct blast mitigation techniques. One promising idea is implementing an adaptive beamformer to suppress the direct

blast. Fully adaptive beamforming presents a challenge however, because the signals are wideband. We are currently investigating the use Steered Covariance Matrices (STCMs) to enable wideband beamforming the TREX13 data [19].

Bibliography

[1] G. Hickman and J. Krolik, "Non-recurrent wideband continuous active sonar," in *Oceans, 2012*, pp. 1–6, Oct 2012.

[2] M. A. Richards, *Fundamentals of radar signal processing: Detection Theory*. New York: McGraw-Hill, 2005.

[3] J. Clancy, H. Bascom, and M. Hartnett, "Mitigation of range folded clutter by a nonrecurrent waveform," in *Radar Conference, 1999. The Record of the 1999 IEEE*, pp. 79–83, 1999.

[4] J. Costas, "A study of a class of detection waveforms having nearly ideal range and doppler ambiguity properties," *Proceedings of the IEEE*, vol. 72, pp. 996–1009, Aug 1984.

[5] N. Levanon and E. Mozeson, "Modified costas signal," *Aerospace and Electronic Systems, IEEE Transactions on*, vol. 40, pp. 946–953, July 2004.

[6] W. Burdic, *Underwater acoustic system analysis*. Englewood Cliffs, NJ: Prentice-Hall, 1984.

[7] S. Kay, *Fundamentals of statistical signal processing: Estimation Theory*. Englewood Cliffs, N.J: Prentice-Hall PTR, 1993.

[8] L. Nolte, "Derivation of the matched filter." Duke University Lecture, October 2012.

[9] S. Kay, *Fundamentals of statistical signal processing*. Englewood Cliffs, N.J: Prentice-Hall PTR, 1993.

[10] Z.-b. Lin, "Wideband ambiguity function of broadband signals," *The Journal of the Acoustical Society of America*, vol. 83, no. 6, 1988.

[11] E. Kelly and R. Wishner, "Matched-filter theory for high-velocity, accelerating targets," *Military Electronics, IEEE Transactions on*, vol. 9, pp. 56–69, Jan 1965.

[12] P. Woodward, *Probability and information theory, with applications to radar*. Dedham, Mass: Artech House, 1980.

[13] N. Levanon, *Radar signals*. Hoboken, New Jersey: John Wiley & Sons, Inc, 2004.

[14] S. Golomb and H. Taylor, "Constructions and properties of costas arrays," *Proceedings of the IEEE*, vol. 72, pp. 1143–1163, Sept 1984.

[15] R. P. Goddard, "The sonar simulation toolset, release 4.6: Science, mathematics, and algorithms," October 2008.

[16] R. Goddard, "The sonar simulation toolset," in *OCEANS '89. Proceedings*, vol. 4, pp. 1217–1222, Sep 1989.

[17] K. Becker and J. Preston, "The onr five octave research array (fora) at penn state," in *OCEANS 2003. Proceedings*, vol. 5, pp. 2607–2610 Vol.5, Sept 2003.

[18] S. Haykin, *Adaptive filter theory*. Upper Saddle River, N.J: Prentice Hall, 2002.

[19] J. Krolik and D. Swingler, "Multiple broad-band source location using steered covariance matrices," *Acoustics, Speech and Signal Processing, IEEE Transactions on*, vol. 37, pp. 1481–1494, Oct 1989.

[20] S. Pecknold, W. Renaud, D. McGaughey, J. Theriault, and R. Marsden, "Improved active sonar performance using costas waveforms," *Oceanic Engineering, IEEE Journal of*, vol. 34, pp. 559–574, Oct 2009.

[21] H. A. DeFerrari, H. B. Nguyen, and A. Rogers, "Continuous active pulse compression sonar," in *Underwater Acoustic Measurements: Technoligies and Results*, (Crete, Greece), 2005.

[22] H. A. DeFerrari, "Ideal signals and processing for continuous active sonar," *J. Acoust. Soc. Am.*, vol. 133, no. 5, p. 3393, 2013.

[23] R. Urick, *Principles of underwater sound for engineers*. New York: McGraw-Hill, 1967.

[24] T. Yang, "Acoustic dopplergram for intruder defense," in *OCEANS 2007*, pp. 1–5, Sept 2007.